

MEASUREMENT OF THE RADIUS OF NEUTRON STARS WITH HIGH S/N QUIESCENT LOW-MASS X-ray BINARIES IN GLOBULAR CLUSTERS

SEBASTIEN GUILLOT *

Department of Physics, McGill University,
3600 rue University, Montreal, QC, Canada, H2X-3R4

MATHIEU SERVILLAT

Laboratoire AIM (CEA/DSM/IRFU/SAP, CNRS, Université Paris Diderot),
CEA Saclay, Bat. 709, 91191 Gif-sur-Yvette, France and
Harvard-Smithsonian Center for Astrophysics, 60 Garden Street, Cambridge, MA 02138, USA

NATALIE A. WEBB

Université de Toulouse; UPS-OMP; IRAP; Toulouse, France and
CNRS; IRAP; 9 Av. colonel Roche, BP 44346, 31028 Toulouse cedex 4, France

ROBERT E. RUTLEDGE

Department of Physics, McGill University,
3600 rue University, Montreal, QC, Canada, H2X-3R4
Accepted to ApJ

ABSTRACT

This paper presents the measurement of the neutron star (NS) radius using the thermal spectra from quiescent low-mass X-ray binaries (qLMXBs) inside globular clusters (GCs). Recent observations of NSs have presented evidence that cold ultra dense matter – present in the core of NSs – is best described by “normal matter” equations of state (EoSs). Such EoSs predict that the radii of NSs, R_{NS} , are quasi-constant (within measurement errors, of $\sim 10\%$) for astrophysically relevant masses ($M_{\text{NS}} > 0.5 M_{\odot}$). The present work adopts this theoretical prediction as an assumption, and uses it to constrain a single R_{NS} value from five qLMXB targets with available high signal-to-noise X-ray spectroscopic data. Employing a Markov-Chain Monte-Carlo approach, we produce the marginalized posterior distribution for R_{NS} , constrained to be the same value for all five NSs in the sample. An effort was made to include all quantifiable sources of uncertainty into the uncertainty of the quoted radius measurement. These include the uncertainties in the distances to the GCs, the uncertainties due to the Galactic absorption in the direction of the GCs, and the possibility of a hard power-law spectral component for count excesses at high photon energy, which are observed in some qLMXBs in the Galactic plane. Using conservative assumptions, we found that the radius, common to the five qLMXBs and constant for a wide range of masses, lies in the low range of possible NS radii, $R_{\text{NS}} = 9.1_{-1.5}^{+1.3}$ km (90%-confidence). Such a value is consistent with low- R_{NS} equations of state. We compare this result with previous radius measurements of NSs from various analyses of different types of systems. In addition, we compare the spectral analyses of individual qLMXBs to previous works.

Subject headings: stars: neutron — X-rays: binaries — globular clusters: individual (ω Cen, M13, M28, NGC 6397, NGC 6304)

1. INTRODUCTION

The relation between pressure and energy density in matter at and above the nuclear saturation density $\rho_c = 2.8 \times 10^{14} \text{ g cm}^{-3}$ is largely unknown (Lattimer & Prakash 2001, 2007). This is mostly due to uncertainties of many-body interactions as well as the unknown nature of strong interactions and symmetry energy. Inside neutron stars (NSs), the equation of state of dense matter ($P(\epsilon)$, written dEoS, hereafter) can be mapped into a mass-radius relation $M_{\text{NS}}(R_{\text{NS}})$ by solving the Tolman-Oppenheimer-Volkoff equation (Oppenheimer & Volkoff 1939; Misner et al. 1973). His-

torically, well before any observational constraints could be placed on the dEoS, nuclear theory attempted to determine the $P(\epsilon)$ relation that would govern the behavior of cold ultra-dense matter. Since the cores of NSs are composed of such matter, its behavior is of astrophysical interest; likewise, the behavior of NSs due to the composition of its core is of nuclear physics interest.

Three main families of dEoSs have been discussed in the last 10–20 years. The first one regroups “normal” dense matter EoSs. At densities at ρ_c , nuclei dissolve and merge, leaving undifferentiated nuclear matter in β -equilibrium. In this type of matter, the pressure is neutron-dominated via the strong force, with a small proton fraction. In other words, NSs are pressure supported against gravity by neutron degeneracy. The “normal” dEoSs are calculated with a relativis-

*Vanier Canada Graduate Scholar
Electronic address: guillots@physics.mcgill.ca
Electronic address: rutledge@physics.mcgill.ca

tic treatment of nucleon-nucleon interactions, leading to a relation between pressure and density, with the pressure vanishing at zero densities (Lattimer & Prakash 2001). For NSs, such dEoSs correspond to $M_{\text{NS}}(R_{\text{NS}})$ lines composed of two parts. One corresponds to constant low M_{NS} at large R_{NS} values. Then, as the density increases, the $M_{\text{NS}}(R_{\text{NS}})$ relation for “normal” dEoSs evolves to quasi-constant¹ R_{NS} as M_{NS} increases, up to a maximum mass, above which the NS collapses to a black-hole. Examples of the proposed form of these dEoSs include AP3-AP4 (Akmal & Pandharipande 1997), ENG (Engvik et al. 1996), MPA1 (Müther et al. 1987), MS0 and MS2 (Müller & Serot 1996), and LS (Lattimer & Swesty 1991).

A second family of dEoSs is characterized by matter in which a significant amount of softening (i.e., less pressure) is included at high densities, due usually to a phase transition at a critical density which introduces an additional hadronic or pure-quark component in what is referred to as the NS’s “inner core”. Additional components, such as a population of hyperons at large densities (GM3, Glendenning & Moszkowski 1991), or kaon condensates (GS1, GS2, Glendenning & Schaffner-Bielich 1999), have been considered. For that reason, these dEoSs are referred to as “hybrid” dense matter. Because of this phase-transition, the maximum M_{NS} is rather low ($M_{\text{NS}} < 1.7 M_{\odot}$). This also results in $M_{\text{NS}}(R_{\text{NS}})$ curves with a smooth decrease in M_{NS} from the maximum to the minimum M_{NS} , as R_{NS} increases. Some of the “hybrid” dEoSs are MS1 (Müller & Serot 1996), FSU (Shen et al. 2010a,b), GM3 (Glendenning & Moszkowski 1991), GS1 (Glendenning & Schaffner-Bielich 1999), and PAL6 (Prakash et al. 1988).

The third family of dEoSs relies on the assumption that strange quarks compose matter in its ground state. One characteristic of such matter is that the pressure vanishes at a non-zero density, compared to the other types of matter described above – they have solid surfaces. In $M_{\text{NS}}-R_{\text{NS}}$ space, these quark star dEoSs follow lines of increasing M_{NS} with increasing radius, up to a maximum radius. Above this value, R_{NS} starts decreasing as M_{NS} increases until M_{NS} reaches its own maximum, where the object collapses to a black-hole. The maximum R_{NS} varies between ~ 9 km and ~ 11 km, depending on the model parameters used, namely, the strange quark mass m_s and the quantum chromodynamic coupling α_c (Prakash et al. 1995). Note that “hybrid” and “normal” matter stars do not have this constraint, and their radii can theoretically be as large as ~ 100 km, at masses $M_{\text{NS}} < 0.5 M_{\odot}$ (Lattimer & Prakash 2001).

Since matter at such densities cannot be produced in Earth laboratories, constraints on the dEoS theoretical models can only be placed by the study of NSs, the only objects in the Universe containing matter at such densities. The measurements of M_{NS} and R_{NS} have the potential to provide great insight to the theory of cold ultra dense matter. Various methods exist to measure M_{NS} and R_{NS} (e.g., Lattimer & Prakash 2007, for a general review). These include the study of quasi-

periodic oscillations in active X-ray binaries (Miller et al. 1998; Méndez & Belloni 2007), Keplerian parameters in NS binaries (Nice et al. 2004; Demorest et al. 2010, for M_{NS} measurements), thermonuclear X-ray bursts (Özel 2006; Suleimanov et al. 2011b, for $M_{\text{NS}}-R_{\text{NS}}$ measurements), pulse-timing analysis of millisecond pulsars (Bogdanov et al. 2008; Bogdanov 2012), and the thermal spectra of quiescent low-mass X-ray binaries (qLMXBs), which is the method of this investigation. Each of these different methods have their own unique systematic uncertainties, and it is therefore of value to pursue each, to permit intercomparison of their conclusions.

By itself, a M_{NS} measurement can only place new constraints on the dEoS when the measured value is above that of all previous M_{NS} measurements. In $M_{\text{NS}}-R_{\text{NS}}$ space, each dEoS predicts a maximum M_{NS} , above which the NS collapses to a black hole. In particular, hybrid dEoSs are characterized by a relatively low maximum M_{NS} ($M_{\text{NS}} < 1.8 M_{\odot}$, Lattimer & Prakash 2001), while normal matter dEoSs produce maximum M_{NS} of up to $2.5 M_{\odot}$ (Lattimer & Prakash 2001). The maximum M_{NS} for strange quark matter (SQM) dEoSs is typically in the vicinity of $2 M_{\odot}$ (Lattimer & Prakash 2001). The maximum M_{NS} property of EoSs can be used to exclude dEoSs. Historically, M_{NS} measurements were in the 1.3–1.5 M_{\odot} range. While the first precise M_{NS} measurements confirmed theoretical predictions about NSs (e.g., Taylor & Weisberg 1989), subsequent measurements at and below previous values did not place any new constraints on the dEoS. Recently, the mass of the radio pulsar PSR 1614–2230 was precisely measured with a value $M_{\text{NS}} = 1.97 \pm 0.04 M_{\odot}$ (Demorest et al. 2010). The implications of this measurement for nuclear physics have been discussed with some depth Lattimer (2011). Such a high M_{NS} excludes previously published hybrid models of dEoSs (using specific values of assumed parameters from within their allowed regions), although it does not rule out any specific form of exotica. SQM dEoSs also seem to be disfavored, since their predicted maximum M_{NS} approaches the $2 M_{\odot}$ limit for only some of the models within the parameter spaces permitted by nuclear physics constraints. Nonetheless, fine tuning of models may allow these disfavored dEoSs to be marginally consistent with the M_{NS} measured in PSR 1614–2230 (for example, Bednarek et al. 2011; Weissenborn et al. 2012, for hybrid models, and Lai & Xu 2011, for SQM models).

Overall, this high- M_{NS} measurement seems to favor “normal matter” hadronic dEoSs. This would mean that the radius of astrophysical NSs should be observed to be within a narrow ($\lesssim 10\%$) range of values for $M_{\text{NS}} > 0.5 M_{\odot}$, since “normal matter” dEoSs follow lines of quasi-constant radius in $M_{\text{NS}}-R_{\text{NS}}$ -space at such masses (Lattimer & Prakash 2001). It is important to notice that the spread in R_{NS} increases for stiff EoSs, especially close to the maximum M_{NS} of the compact object (e.g., up to a 2-km difference in R_{NS} for the EoS PAL1, Prakash et al. 1988).

The empirical dEoS obtained from $M_{\text{NS}}-R_{\text{NS}}$ confidence regions from type-I X-ray bursts and from the thermal spectra of qLMXBs combined also favors this conclusion (Steiner et al. 2010, 2012). Using a Bayesian approach, the most probable dEoS was calculated, resulting in a dEoS approaching the behavior of theoret-

¹ Here, and elsewhere, we use the term “quasi-constant” to mean constant within measurement precision, $\sim 10\%$. This should be differentiated from a value which is constant when measured with infinite precision, or a value which is constant according to theory.

ical hadronic dEoSs, with predicted radii in the range $R_{\text{NS}} \sim 10 - 13$ km. Such radii suggest that soft hadronic dEoSs are describing the dense matter inside NSs. However, different analyses of other NSs found radii consistent with stiff dEoSs. These include the qLMXB X7 in 47Tuc (Heinke et al. 2006), or the type I X-ray burster 4U 1724-307 (Suleimanov et al. 2011a). Nonetheless, these results are not inconsistent with the observation that the R_{NS} is almost constant for a large range of M_{NS} , since they are consistent with stiff “normal matter” dEoSs, such as MS0/2 (Müller & Serot 1996)

Given the evidence supporting the “normal matter” hadronic dEoSs, it therefore becomes a natural assumption – to be tested against data – that observed NSs have radii which occupy only a small range of R_{NS} values ($\lesssim 10\%$). Using the thermal spectra of five qLMXBs, fitted with a H-atmosphere model, a single R_{NS} value is assumed and measured, as well as its uncertainty. Furthermore, under this assumption, the best-fit M_{NS} and surface effective temperature kT_{eff} for these qLMXBs and their uncertainties are extracted. The various sources of uncertainty involved in this spectral analysis are addressed, including, the distances to the qLMXBs, the amount of galactic absorption in their direction, and the possibility of an excess of high-energy photons as observed for other qLMXBs (and modeled with a power-law component, PL hereafter). The goal is to place the best possible constraints on R_{NS} accounting for all known uncertainties, and eliminating all unquantifiable systematic uncertainties.

In this article, we provide the necessary theoretical background and observational scenario to understand $M_{\text{NS}}-R_{\text{NS}}$ measurements of NSs from qLMXBs (§ 2). The organization of the rest of the paper is as follows: Section 3 explains the analysis of the X-ray data. Section 4 contains the results of the spectral analysis. A discussion of the results is in Section 5 and a summary is provided in Section 6.

2. QUIESCENT LOW-MASS X-RAY BINARIES

The low-luminosity of qLMXBs was initially observed following the outbursts of the X-ray transients Cen X-4 and Aql X-1 (van Paradijs et al. 1987). This faint emission ($L_{\text{X}} \sim 10^{32} - 10^{33}$ erg s $^{-1}$, 4-5 orders of magnitude fainter than during outburst) was originally interpreted as a thermal blackbody emission. Low-level mass accretion onto the compact object was thought to explain the observed luminosity (Verbunt et al. 1994).

Later, an alternative to the low-level accretion hypothesis was proposed. This alternate theory, which became the dominant explanation for the emission from qLMXBs, suggests that the observed luminosity is provided, not by low- \dot{M} , but by the heat deposited in the deep crust during outbursts (Brown et al. 1998). In the theory of deep crustal heating (DCH), the matter accreted during an outburst releases ~ 1.9 MeV of energy via pressure-sensitive reactions: electron captures, neutron emissions or pycnonuclear reactions (Sato 1979; Haensel & Zdunik 1990; Gupta et al. 2007; Haensel & Zdunik 2008). Therefore, the time-averaged quiescent luminosity is proportional to the time-averaged

mass accretion rate:

$$\langle L \rangle = 9 \times 10^{32} \frac{\langle \dot{M} \rangle}{10^{-11} M_{\odot} \text{ yr}^{-1}} \frac{Q}{1.5 \text{ MeV/amu}} \text{ erg s}^{-1} \quad (1)$$

where Q is the average heat deposited in the NS crust per accreted nucleon (Brown et al. 1998; Brown 2000).

Following this hypothesis about the energy source of the quiescent luminosity, the theory of DCH also explains the observed spectra of qLMXBs. As a result of the energy deposited in the deep crust, the core heats up during the outbursts. The energy is then re-radiated on core-cooling time scales away from the crust, and through the NS atmosphere (Brown et al. 1998). The NS atmosphere is assumed to be composed of pure hydrogen. Indeed, at the accretion rates expected during quiescence, heavier elements settle on time scales of order \sim seconds (Romani 1987; Bildsten et al. 1992). The possibility of helium (He) or carbon atmospheres around NSs in LMXBs has also been studied (Ho & Heinke 2009; Servillat et al. 2012).

Several models of H-atmosphere around NSs have been developed (Rajagopal & Romani 1996; Zavlin et al. 1996; McClintock et al. 2004; Heinke et al. 2006; Haakonsen et al. 2012). They are now routinely used to explain the emergent spectra of qLMXBs, with emission area radii compatible with the entire surface area of NSs, compared to derived emission area radii of $\lesssim 1$ km in the blackbody interpretation (Rutledge et al. 1999). The DCH theory and H-atmosphere models were first applied to explain the quiescent spectra and measure the radius of historically transient LMXB (e.g., Cen X-4, Campana et al. 2000; Rutledge et al. 2001a, Aql X-1, Rutledge et al. 2001b). However, the 10-50% systematic uncertainty on the distance to field LMXBs directly contributes to a 10-50% uncertainty on the radius measurements. Due to these large systematic uncertainties, these objects provide limited use to place constraints on the dEoS until more precise measurements of their distances can be obtained.

Placing tight constraints on the dEoS requires $\sim 5\%$ uncertainty on the R_{NS} measurements. This constraint is approximately the half-width of the range of radii in the $M_{\text{NS}}(R_{\text{NS}})$ relationships corresponding to “normal matter” EoSs. Globular clusters (GCs) have properties which make them ideal targets for qLMXB observations: relatively accurately measured distances; better characterized Galactic absorption; over-abundances of LMXBs; and LMXBs with magnetic field weak enough that the thermal spectrum is not affected (Heinke et al. 2006). A handful of qLMXBs have been discovered in GCs so far; only a few have X-ray spectra with the high signal-to-noise ratio (S/N) necessary to measure R_{NS} with $\lesssim 10 - 15\%$ uncertainty, including the uncertainty to their distances.

3. DATA REDUCTION AND ANALYSIS

3.1. Targets

The targets used in this work are chosen among the qLMXBs located in GCs that produced the best R_{NS} measurements, i.e., with R_{∞} uncertainties of $\lesssim 15\%$ in the previous works.

The GCs ω Cen (Rutledge et al. 2002; Gendre et al. 2003a) and M13 (Gendre et al. 2003b; Catuneanu et al.

TABLE 1
X-RAY EXPOSURES OF THE TARGETED CLUSTERS.

Target	Obs. ID	Starting Time (TT)	Usable time (ksec)	S/N	Telescope and detector	Filter or Mode	Refs.
M28	2683	2002 July 04 18:02:19	14.0	23.85	<i>Chandra</i> ACIS-S3 (BI)	VFAINT	2
M28	2684	2002 Aug. 04 23:46:25	13.9	23.54	<i>Chandra</i> ACIS-S3 (BI)	VFAINT	2
M28	2685	2002 Sep. 09 16:55:03	14.3	23.90	<i>Chandra</i> ACIS-S3 (BI)	VFAINT	2
M28	9132	2008 Aug. 07 20:45:43	144.4	78.75	<i>Chandra</i> ACIS-S3 (BI)	VFAINT	1, 3
M28	9133	2008 Aug. 10 23:50:24	55.2	48.46	<i>Chandra</i> ACIS-S3 (BI)	VFAINT	1, 3
NGC 6397	79	2000 July 31 15:31:33	48.34	25.03	<i>Chandra</i> ACIS-I3 (FI)	FAINT	4, 5
NGC 6397	2668	2002 May 13 19:17:40	28.10	25.47	<i>Chandra</i> ACIS-S3 (BI)	FAINT	5
NGC 6397	2669	2002 May 15 18:53:27	26.66	24.97	<i>Chandra</i> ACIS-S3 (BI)	FAINT	5
NGC 6397	7460	2007 July 16 06:21:36	149.61	52.31	<i>Chandra</i> ACIS-S3 (BI)	VFAINT	5
NGC 6397	7461	2007 June 22 21:44:15	87.87	41.40	<i>Chandra</i> ACIS-S3 (BI)	VFAINT	5
M13	0085280301	2002 Jan. 28 01:52:41	18.8	14.25	<i>XMM</i> pn, MOS1, MOS2	Medium	6,7
M13	0085280801	2002 Jan. 30 02:21:33	17.2	12.10	<i>XMM</i> pn, MOS1, MOS2	Medium	6,7
M13	5436	2006 Mar. 11 06:19:34	27.1	16.07	<i>Chandra</i> ACIS-S3 (BI)	FAINT	1,8
M13	7290	2006 Mar. 09 23:01:13	28.2	16.01	<i>Chandra</i> ACIS-S3 (BI)	FAINT	1,8
ω Cen	653	2000 Jan. 24 02:13:28	25.3	13.33	<i>Chandra</i> ACIS-I3 (FI)	VFAINT	9
ω Cen	1519	2000 Jan. 25 04:32:36	44.1	16.45	<i>Chandra</i> ACIS-I3 (FI)	VFAINT	9
ω Cen	0112220101	2001 Aug. 12 23:34:44	33.9	24.35	<i>XMM</i> pn, MOS1, MOS2	Medium	7,10
NGC 6304	11074	2010 July 31 15:31:33	98.7	27.94	<i>Chandra</i> ACIS-I3 (FI)	VFAINT	1

NOTE. — TT refers to Terrestrial Time. FI and BI refers to the front-illuminated and back-illuminated ACIS chips. References: (1) This work; (2) Becker et al. (2003); (3) Servillat et al. (2012); (4) Grindlay et al. (2001); (5) Guillot et al. (2011a); (6) Gendre et al. (2003b); (7) Webb & Barret (2007); (8) Catuneanu et al. (2013), (9) Rutledge et al. (2002); (10) Gendre et al. (2003a); All observations have been re-processed and re-analyzed in this work. The references provided here are given to indicate the previously published analyses of the data.

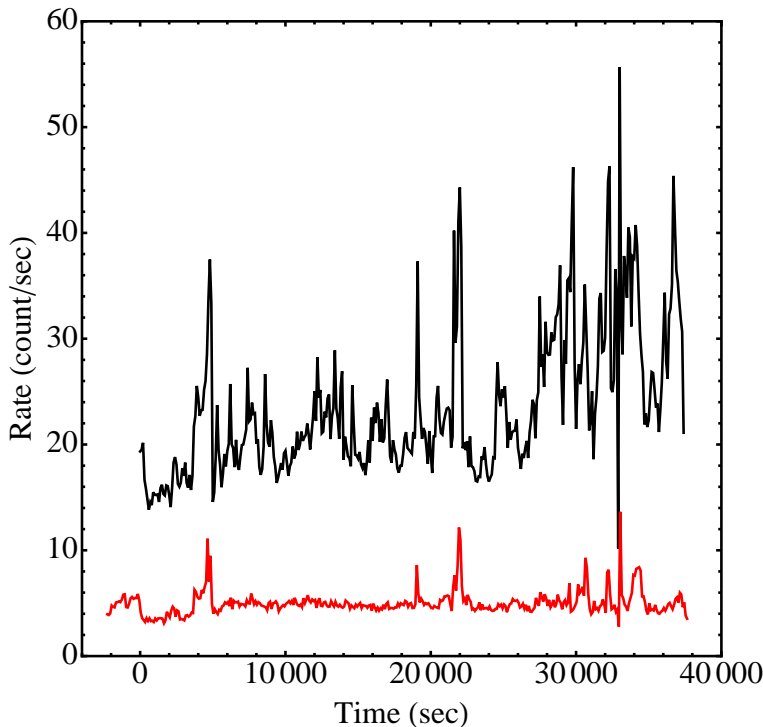


FIG. 1.— Figure showing the *XMM*-pn full-detector light curves of ω Cen, ObsID 0112220101, with bins of 100 sec. The black (top) line corresponds to the pn camera light curve. The $t = 0$ sec time is the beginning of the pn exposure, on 2001 Aug. 12, 23:34:44. The MOS1 light curve, in red (bottom), is shown for completeness and because periods of flaring are more readily visible. The time intervals with large background flaring are excluded from the analyzed data set.

2013) each have one qLMXB that was used in previous work to place moderate constraints on the dEoS (Webb & Barret 2007). The projected radius measure-

ments R_∞ reported in the original works are within 2–3% uncertainty. However, there is evidence that these uncertainties are highly under-estimated (§ 4).

The qLMXB in the core of NGC 6304, discovered recently with the *XMM-Newton* observatory (*XMM*, hereafter) and confirmed with a short *Chandra X-ray Observatory* exposure (Guillot et al. 2009a,b), was then observed for 100 ks with ACIS-I onboard *Chandra* (Advanced Charge-coupled-device Imaging Spectrometer). In this work, only the long *Chandra* exposure is used since, in the *XMM* observation, the core source is contaminated by nearby sources, mostly one spectrally hard source (Guillot et al. 2009b).

The qLMXB in NGC 6397 (named U24 in the discovery observation, Grindlay et al. 2001) has a R_{NS} value measured with $\sim 8\%$ uncertainty, obtained from a total of 350 ks of *Chandra X-ray Observatory* archived observations (Guillot et al. 2011a). The spectra for this target were re-analyzed in this work, for a more uniform analysis.

Finally, the R_∞ measurement of the NS qLMXB in the core of M28 reported in the discovery observation does not place useful constraints on the dEoS: $R_\infty = 14.5^{+6.9}_{-3.8}$ (Becker et al. 2003). However, an additional 200 ks of archived observations with *Chandra* have been analyzed in a recent work, finding $R_{\text{NS}} = 9 \pm 3$ km and $M_{\text{NS}} = 1.4^{+0.4}_{-0.9} M_\odot$ for a H-atmosphere, and $R_{\text{NS}} = 14^{+3}_{-8}$ and $M_{\text{NS}} = 2.0^{+0.5}_{-1.5} M_\odot$ for a pure He-atmosphere (Servillat et al. 2012, and their Figures 3 and 4, for the $M_{\text{NS}}-R_{\text{NS}}$ confidence regions). The same data sets are used in the present work. This source is moderately piled-up ($\sim 4\%$ pile-up fraction) and necessitates the inclusion of a pile-up model component (Davis 2001, see § 3.4 for details). All uncertainties for values obtained from a X-ray spectral analysis with *XSPEC* are quoted at the 90% confidence level, unless noted otherwise.

The qLMXB X7 in 47 Tuc has also been observed with

the high S/N that could provide constraints on the dEoS. However, it suffers from a significant amount of pile-up (pile-up fraction $\sim 10\text{--}15\%$). While the effects of pile-up can be estimated and corrected for by the inclusion of a pile-up model (Heinke et al. 2003, 2006), the uncertainties involved with such a large amount of pile-up are not quantified in this model². It was chosen not to include this target in the present analysis, in an effort to limit the sources of uncertainties that are not quantified (see § 3.4).

The list of targets and their usable observations with *XMM* and *Chandra* is presented in Table 1, along with the usable exposure time and other relevant parameters of the observations.

3.2. Data Processing

The processing of raw data sets is performed according to the standard reduction procedures, described briefly below.

3.2.1. Chandra X-ray Observatory Data Sets

The reduction and analysis of *Chandra* data sets (ACIS-I or ACIS-S) is done using CIAO v4.4. The level-1 event files were first reprocessed using the public script *chandra_repro* which performs the steps recommended in the data preparation analysis thread³ (charge transfer inefficiency corrections, destreaking, bad pixel removal, etc, if needed) making use of the latest effective area maps, quantum efficiency maps and gain maps of CALDB v4.4.8 (Graessle et al. 2007). The newly created level-2 event files are then systematically checked for background flares. Such flares were only found in the middle and at the end of an observation of M28 (ObsID 2683), for a total of 3ks. These two flares caused an increase by a factor of 2.4, at most, of the background count level. Given the extraction radius chosen here (see below), this period of high background contaminates the source region with < 1 count. Therefore, the entire exposure of the ObsID is included in the present analysis.

To account for the uncertainties of the absolute flux calibration, we add systematics to each spectral bins using the *heasoft* tool *grppha*. In the 0.5–10 keV range, we add 3% systematics (Table 2 in Chandra X-Ray Center Calibration Memo by Edgar & Vikhlinin 2004). This document (Table 2) provides the uncertainties on the ACIS detector quantum efficiency at various energies, which are 3% at most. In the 0.3–0.5 keV range, the uncertainty in the calibration is affected by the molecular contamination affecting ACIS observations. The recent version of CALDB contains an improved model for this contamination. The RMS residuals are now limited to 10% in the 0.3–0.5 keV range (Figure 15 of document “Update to ACIS Contamination Model”, Jan 8, 2010, ACIS Calibration Memo⁴). To account for the variations in the residuals of contamination model, we add 10% systematics to spectral bins below 0.5 keV.

3.2.2. XMM-Newton Data Sets

The reduction of *XMM* data sets is completed using the *XMM Science Analysis System v10.0.0* with standard procedures. The command *epchain* performs the preliminary data reduction and creates the event files for the pn camera in the 0.4–10.0 keV energy range, with 3% systematic uncertainties included, accounting for the uncertainties in the flux calibration of the pn camera on *XMM* (Guainizzi 2012). The data sets are checked for flares and time intervals with large background flares are removed. The total usable time (after flare removal) for each observation is listed in Table 1. MOS1 and MOS2 data are not used in the present work to minimize the effects of cross-calibration uncertainties between detectors.

3.3. Count Extraction

3.3.1. On Chandra X-ray Observatory Data Sets

The count extraction of the source and background spectra is performed with the task *specextract*, as well as the calculation of the response matrices and ancillary response files (RMFs and ARFs). The centroid position is chosen using the reported source positions from previous works. The extraction radii are chosen to correspond to a 99% EEf (Encircled Energy Fraction), and therefore depend on the off-axis angle of the targets. For on-axis qLMXBs (M13, M28, NGC 6397 and NGC 6304), counts within a $3.4''$ radius are extracted to create the spectrum. This ensures that 99% of the enclosed energy fraction at 1 keV is included⁵. The qLMXB in ω Cen is at a large off-axis angle ($\sim 4.4'$) which requires an extraction radius of $6''$ to contain 99% of the EEf. This is due to the degradation of the PSF of the *Chandra* mirror with increasing off-axis angle. Background counts were taken from an annulus centered around the qLMXB, with an inner radius of $5''$ ($9''$ for ω Cen) and an outer radius of $50''$. Regions surrounding other point sources detected in the qLMXB extraction regions or in the background regions are also excluded (radius of $5''$ or more). For NGC 6304, the background region is off-centered with respect to the source region, to ensure that the background lies on the same CCD chip as the source.

Figures 2a–e show the regions used to extract the counts and create the spectra of each target. When several observations are available for a target, the largest-S/N observation was used to create the figure.

3.3.2. On XMM-Newton Data Sets

For the three *XMM* data sets, the extraction method was the same as that described above. Only the source extraction radii were different and determined using the XMM SAS task *eregionanalyse* which provides the optimum extraction radius that maximizes the S/N given the source position and the surrounding background. The optimum radius is $19''$ for ObsID 01122 of ω Cen. The encircled energy of the source is therefore 79% at 1.5 keV.

For the *XMM* observations of M13, the close proximity of a cataclysmic variable (CV) complicates the task. A $25''$ extraction radius and a $12.5''$ exclusion radius for the nearby source are used to create the spectra. It ensures

² See “The Chandra ABC Guide to Pile-Up” available at http://cxc.harvard.edu/ciao/download/doc/pileup_abc.pdf

³ <http://cxc.harvard.edu/ciao/threads/data.html>

⁴ available at http://cxc.harvard.edu/cal/memos/contam_memo.pdf

⁵ *Chandra* Observatory Proposer Guide v15.0, fig. 6.7, December 2012

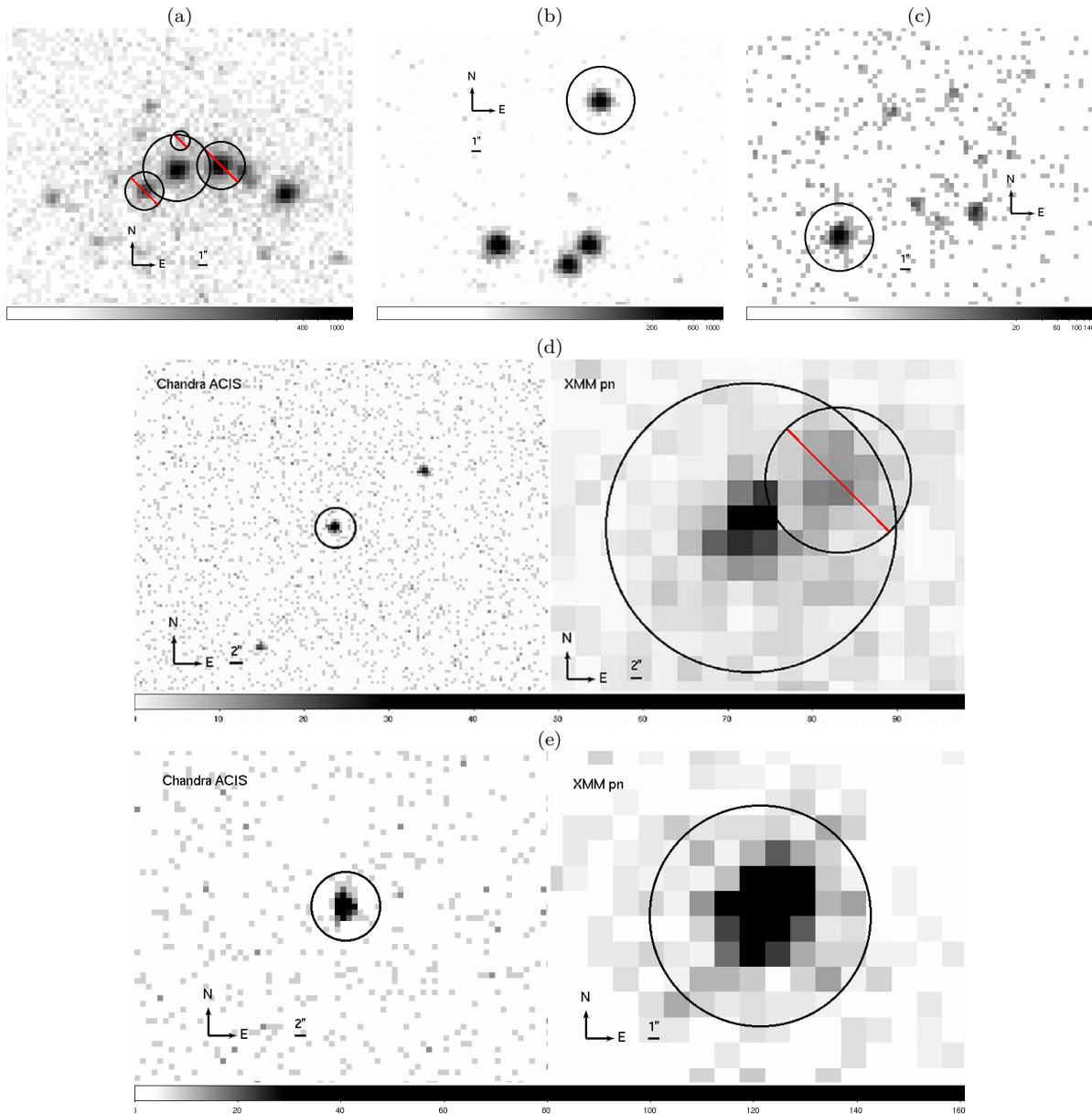


FIG. 2.— Figure showing the extraction regions for the five qLMXBs. (a) For M28, ObsID 9132, the three nearby sources are excluded, limiting contamination to $< 1\%$ within the extraction region (see Table 2). (b) For NGC 6397, ObsID 7460, no counts from nearby sources fall within the extraction region. (c) For NGC 6304, ObsID 11074, the nearby sources are not contaminating the extraction region. (d) For M13, *Chandra* data are on the left, ObsID 7290, and *XMM* data are on the right, ObsID 0085280301. The nearby CV is excluded. (e) For ω Cen, *Chandra* data are on the left, ObsID 1519, and *XMM* data are on the right, ObsID 0112220101. There is no contamination from nearby sources.

that 84% of the total energy from the qLMXB at 1.5 keV is encircled⁶.

Similar to the *Chandra* data, the background is an annulus around the source, restricted to remain on the same CCD chip as the source. `rmfgen` and `arfgen` are then used to generate the response matrices files (RMF) and the ancillary response file (ARF) for each observations.

3.3.3. Contamination from Nearby Sources

As mentioned above, some qLMXBs lie in close proximity of other contaminating sources. The most evident case is that of M13, observed with *XMM* (Figure 2e), in which part of the counts from a nearby CV still overlaps

with the qLMXB extraction region even after excluding $10''$ around the CV. In M28, three sources in the proximity of the qLMXB require parts of the extraction region to be excluded (Figure 2a), with a minor contamination from the nearby sources. For the observations of M28 and M13, the fraction of contaminating counts present within the extraction region of the qLMXBs is estimated using a Monte Carlo sampler which draws counts from the radial distribution of encircled energy of ACIS or pn at 1 keV (see footnotes in previous subsections). Table 2 lists the amount of contamination for each observation of M28 and for the *XMM*-pn observations of M13. The contamination over the M28 qLMXB region can be neglected, since, in the worst case (ObsID 9132) only 47 counts out

⁶ From *XMM* Users Handbook, fig. 3.7, July 2010

of 6250 are contamination from nearby sources. The CV close to the qLMXB in M13 causes a contamination of 6% and 9% of the counts in each of the *XMM* spectra, or 4% of the total counts available for the qLMXB in M13 (*XMM* and *Chandra* spectra combined). Overall, contamination for nearby sources represents 0.5% of the total count number, all sources combined. This contamination can be safely neglected, since it will not significantly affect the radius measurement.

3.4. Pile-Up

Observations of bright X-ray sources may be subject to an instrumental effect known as pile-up. When two or more photons strike a pixel on an X-ray detector within a single time frame (3.24 sec for *Chandra*-ACIS observations and 73.4 ms for *XMM*-pn observations), the pile-up effect causes degradation of the PSF and, more importantly for the analysis presented here, a degradation of the spectral response. Specifically, the recorded energy of the event will be the sum of the two (or more) piled-up photon energies. In addition, grade migration (also called photon pattern distortion for *XMM*) also occurs. Although a pile-up model exists in *XSPEC* to take into account these effects (Davis 2001), it is chosen here to restrict the analysis to mildly piled-up observations.

None the *XMM* observations of qLMXBs are piled-up, given the short duration of a single time frame on *XMM*-pn (73.4 ms). Quantitatively, the count rates of the qLMXBs in ω Cen and M13 (2.6×10^{-2} and 2.7×10^{-2} counts per seconds, respectively) correspond to $\sim 10^{-3}$ counts per frame. At those rates, the pile-up is negligible. The frame time of *Chandra*-ACIS in full-frame mode, however, is significantly longer than that of *XMM*-pn (compensated by the smaller effective area). The *Chandra* observations of the qLMXB in M28 are moderately piled-up because of a count rate of ~ 0.043 counts per seconds (~ 0.14 counts per frame) which corresponds to a pile-up fraction of $\sim 5\%$ ⁷. Such amount of pile-up cannot be neglected and is taken into account using the `pileup` model in *XSPEC* (Davis 2001). Other *Chandra* observations of the qLMXBs studied in this work have smaller count rates which do not necessitate a pile-up correction.

As stated before, the correction of pile-up fractions $\sim 10\%$ and above (such as that of the qLMXB in 47Tuc, observed in full-frame mode on *Chandra*/ACIS) comes with unquantified uncertainties. This is tested by simulating piled-up spectra of 47Tuc (10–15% pileup fraction) and M28 (5% pileup fraction) with their respective `nsatmos` parameters, and then by fitting the spectra with the `nsatmos` model without the pile-up component. The best-fit radii of each spectrum is affected by systematics: $\sim 10\%$ for M28 and $\sim 50\%$ for 47Tuc. The systematic error involved with the pile-up of M28 is smaller than the measurement error of R_{NS} in the present analysis, while for 47Tuc, the systematic bias caused by pileup is substantially larger than the R_{NS} measurement uncertainty. Therefore, the qLMXB in 47Tuc is not used in this analysis to avoid introducing a systematic uncertainty which may be comparable in size to our total statistical uncer-

TABLE 2
COUNT CONTAMINATION FROM NEARBY SOURCES

Target	ObsID (detector)	Number of contaminating counts				Total (%)
		source 1	source 2	source 3	sum	
M28	2693 (ACIS)	0.16	0.11	0.16	0.43	0.08%
	2684 (ACIS)	0	0.15	0.32	0.47	0.08%
	2685 (ACIS)	0.05	0.19	0.17	0.37	0.06%
	9132 (ACIS)	1.7	38.9	6.3	46.9	0.75%
	9133 (ACIS)	1.0	11.7	2.7	15.4	0.65%
M13	0085280301 (pn)	27	–	–	27	8.7%
	0085280801 (pn)	34	–	–	34	6.2%

NOTE. — The columns “source1”, “source2” and “source3” indicate the absolute numbers of counts falling within the qLMXB extraction region, and “sum” is the simple sum of contaminating counts. For M13, there is only one nearby source, not fully resolved with *XMM*. The last column provides the amount of contamination as a percent of the total number of counts within the qLMXB extraction region. tainty⁸.

3.5. Spectral Analysis

The spectral analysis is composed of two parts. In the first one, the five targets are analyzed individually and the results are compared to previously published results. The second part of the analysis in the present work pertains to the simultaneous fitting of the targets, with a R_{NS} value common to all five qLMXBs. Prior to the discussion of these two parts, the analysis techniques common to the two analyses are described.

3.5.1. Counts Binning, Data Groups and Model Used

Once the spectra and the respective response files of each observation are extracted, the energy channels are grouped with a minimum of 20 counts per bin to ensure that the Gaussian approximation is valid in each bin. For observations with a large number of counts (>2000 counts, in ObsID 9132 and 9133 of M28 and ObsID 7460 of NGC 6397), the binning is performed with a minimum of 40 counts per bin. In all cases, when the last bin (at high energy, up to 10 keV) contains less than 20 counts, the events are merged into the previous bin.

The spectral fitting is performed using the “data group” feature of *XSPEC*. The spectra of each target are grouped together, and each group (corresponding to each qLMXB) is assigned the same set of parameters. The spectral model used is the `nsatmos` model (Heinke et al. 2006), together with Galactic absorption taken into account with the multiplicative model `wabs`. The amounts of Galactic absorption, parameterized by N_H ($N_{H,22}$ in units of 10^{22} atoms cm^{-2} , hereafter), are fitted during the spectral analysis, and compared to those obtained from a HI Galactic survey from NRAO data⁹ (Dickey & Lockman 1990). The N_H values used in the present analysis are shown in Table 3. The results obtained with `nsatmos` are also compared with the best-fit results using the model `nsagrav` (Zavlin et al. 1996) for completeness.

As mentioned before, the `pileup` model (Davis 2001) is necessary for the spectral fitting of M28 spectra. In

⁸ Note that we find in Section 5.2.2 that inclusion of 47Tuc X7 in this analysis does not significantly affect our best-fit R_{NS} value; nonetheless, we do not include this data, since we cannot estimate the effect of including it on our error region.

⁹ obtained from the *HEASARC* N_H tools available at <http://heasarc.nasa.gov/cgi-bin/Tools/w3nh/w3nh.pl>

⁷ *Chandra* Observatory Proposer Guide v12.0, fig. 6.18, December 2009

XSPEC, multiple groups cannot be fitted with different models, so a single model is applied to all groups, namely, `pileup*wabs*nsatmos`. For the spectra of the qLMXB in M28, the α parameter of the `pileup` model, called “good grade morphing parameter” is left free. The frame time parameter is fixed at 3.10 sec. This value corresponds to the `TIMDEL` parameter of the header (3.14104 sec for the observations of M28) where the read-out time (41.04 ms) is subtracted. All the other parameters of the `pileup` model are held fixed at their default values, as recommended in the document “The Chandra ABC Guide to Pile-Up v.2.2”¹⁰. Since the targets in M13, ω Cen, NGC 6397 and NGC 6304 do not require to account for pile-up, the time frame for these four groups is set to a value small enough so that the `pileup` model has essentially no effect and the α parameters of the four non piled-up sources are kept fixed at the default value, $\alpha = 1$. A quick test is performed to demonstrate that the `pileup` model with a small frame time has no effect on the spectral fit using the non piled-up spectra of the qLMXB in NGC 6304. Specifically, the best-fit `nsatmos` parameters and the χ^2 -statistic do not change when the `pileup` model (with a frame time of 0.001 sec) is added, as expected.

3.5.2. Individual Targets

Prior to the spectral analysis, it is important to verify that the qLMXBs do not present signs of spectral variability. This is done by considering each target individually (without the other targets) and by demonstrating that the `nsatmos` spectral model fits adequately, with the same parameters, all the observations of the given target. More precisely, for each target, all the parameters are tied together and we verify that the fit is statistically acceptable.

In Section 4.1, the results of the spectral fits of individual targets are presented. In order to provide the full correlation matrix for all the parameters in the fit, a Markov-Chain Monte-Carlo (MCMC) simulation is implemented (described in § 3.6) and the resulting posterior distributions are used as the best-fit confidence intervals, including the $M_{\text{NS}}-R_{\text{NS}}$ confidence region. These spectral fitting simulations are performed with the Galactic absorption parameters N_H left free. This allows us to obtain best-fit X-ray-measured values of the absorption in the direction of each of the targeted GCs. These best-fit values are compared to HI-deduced values (from neutral hydrogen surveys), and are also used for the remainder of the work, when N_H is kept fixed. Finally, the results of the individual spectral fits are compared to previously published results.

3.5.3. Simultaneous Spectral Analysis of the Five Targets

The main goal of this paper is the simultaneous spectral fit of five qLMXBs assuming an R_{NS} common to all qLMXBs. Therefore, R_{NS} is a free parameter constrained to be the same for all data sets, while each NS targeted has its own free M_{NS} and kT_{eff} parameters. In addition, the spectra of M28 require an extra free parameter α for the modeling of pile-up. This leads to a total of 12 free parameters.

In an effort to include all possible uncertainties in the production of the $M_{\text{NS}}-R_{\text{NS}}$ confidence regions, Gaussian Bayesian priors for the source distances parameters are included, instead of keeping the parameter values fixed¹¹. Since, additional systematic uncertainties can arise when keeping the N_H parameters fixed, this assumption is also relaxed in the spectral analysis. Finally, the spectra of some qLMXBs display excess flux above 2 keV, which is not due to the H-atmosphere thermal emission. This is accounted for by adding a PL spectral component to the model, where the photon index is fixed at $\Gamma = 1.0$ but the PL normalizations are free to vary. Such PL index is the hardest observed for a LMXB in quiescence (Cen X-4 Cackett et al. 2010). The spectra resulting from this analysis (with all five qLMXBs, and with all assumptions relaxed) are shown in Figure 3.

Relaxing the assumptions mentioned above adds 15 free parameters, for a total of 27, which increases the complexity of the χ^2 -space. Because of that, in *XSPEC*, the estimation of the confidence region for each parameter proves difficult. The command `steppar` iteratively calculates the χ^2 -value for fixed values of a parameter in the range provided by the user. However, this grid-search procedure is highly dependent on the starting point of the parameter of interest and on the number of steps. Such a problem is particularly evident in the case of highly covariant sets of parameters. This can result in 1D or 2D $\Delta\chi^2$ contours that are not reliable to estimate the uncertainties. A solution to this issue consists of using the posterior distributions from MCMC simulations (described in § 3.6). With those, one can quantify the uncertainties of each parameters. The need to include Bayesian priors also brings forward the use of MCMC simulations.

The simultaneous spectral fitting of all five targets using MCMC simulations was performed in seven separate runs, during which the assumptions on the spectral model are progressively relaxed. The characteristics of each run are described in Section 4.2. Another run is also performed with the `nsagrav` model for purposes of comparison with the `nsatmos` model. The following subsection describes the MCMC analysis performed.

3.6. Markov-Chain Monte Carlo Analysis

As described above, the main advantage of using an MCMC simulation resides in a complete understanding of the posterior probability density functions of each parameter. It also allows one to marginalize over the so-called nuisance parameters, i.e., those that are an important part of the modeling but which are of little physical interest to the problem at hand.

Because of the curved parameter distributions obtained with the `nsatmos` model, in particular the $M_{\text{NS}}-R_{\text{NS}}$ contours, an MCMC algorithm different from the typically used Metropolis-Hasting algorithm (MH) is chosen. Indeed, we find that the MH algorithm is not efficient at exploring skewed parameter spaces. The next few paragraphs are dedicated to a brief description of the Stretch-Move algorithm used.

The Stretch-Move algorithm (Goodman & Weare 2010) is particularly useful for elongated and curved distributions (e.g., $M_{\text{NS}}-R_{\text{NS}}$ with `nsatmos`), as demonstrated in previous works (e.g., Wang et al. 2011); our

¹⁰ from the Chandra X-ray Science Center (June 2010), available at http://cxc.harvard.edu/ciao/download/doc/pileup_abc.pdf

¹¹ For a review on Bayesian analysis, see Gregory (2005)

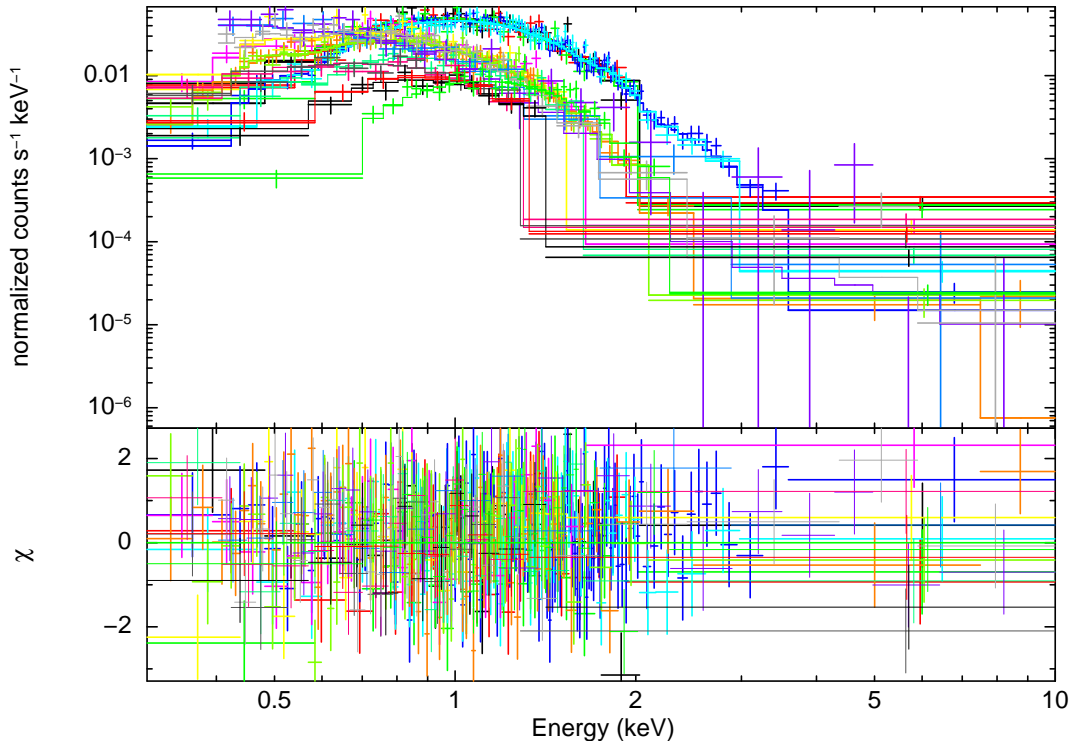


FIG. 3.— Figure showing the spectra resulting from Run #7, obtained with the model `wabs*(nsatmos+pow)`, for which the best-fit statistic is χ^2/dof (prob.) = 0.98/628 (0.64).

implementation generally follows that work. Other analyses have used the Stretch-Move algorithm (Bovy et al. 2012; Olofsson et al. 2012, using another implementation, by Foreman-Mackey et al. 2012). The algorithm consists of running several simultaneous chains, also called walkers, where the next iteration for each chain is chosen along the line connecting the current point of the chain and the current point of another randomly selected chain. The amount of “stretching” is defined by a random number z from an affine-invariant distribution (Goodman & Weare 2010):

$$g(z) \propto \begin{cases} \frac{1}{\sqrt{z}} & \text{if } z \in [\frac{1}{a}, a] \\ 0 & \text{otherwise} \end{cases} \quad (2)$$

In this work, each individual chain starts from a randomly selected point in the parameter space, within the typical hard limits defined for `nsatmos` in *XSPEC*.

The parameter a is used as a scaling factor and is adjusted to improve performance. A larger value of a increases the “stretching” of the chains, i.e., the algorithm will better explore the elongated parts of the parameter space, but it decreases the likelihood that the next step is accepted. A smaller value of a only produces small excursions from the previous value but increases the likelihood that the next step is accepted. Efficiency is optimized at an intermediate value of a . The Stretch-Move algorithm can be fine-tuned with only two parameters: a and the number of simultaneous chain. By comparison, the MH algorithm requires $N(N+1)/2$ tuning variables, where N is the number of free parameters.

The validity of this MCMC algorithm is assessed by performed a test run with a single source (U24 in

NGC 6397, with fixed distance) and comparing the resulting $M_{\text{NS}}-R_{\text{NS}}$ contours with those obtained from a simple grid-search method (`steppar` in *XSPEC*). Specifically, the obtained $M_{\text{NS}}-R_{\text{NS}}$ contours as well as other posterior distributions match those obtained from a `steppar` grid-search in *XSPEC*. The addition of Gaussian Bayesian priors on the distance is also tested with U24, which results in $M_{\text{NS}}-R_{\text{NS}}$ contours broadened in the R_{∞} direction. This is because the normalization of the thermal spectrum is approximately $\propto (R_{\infty}/d)^2$.

For the Stretch-Move algorithm, the minimum number of simultaneous chains is equal to $N+1$, where N is the number of free parameters. However, increasing the number of simultaneous chains ensures a more complete coverage of the parameter space, when comparing the results of the Stretch-Move algorithm to contours obtained with `steppar`. In addition, it reduces the chances of having the $N+1$ walkers collapsing to a $N-1$ dimensional space, i.e., one of the parameters has the same value within all the chains causing all following steps to evolve in the same plane. However, increasing the number of walkers also increases the convergence time.

The resulting posterior distributions are then marginalized over nuisance parameters. While necessary for the spectral fitting, these parameters do not provide physical information (e.g., α , the pile-up parameter). The results are presented in Section 4, where the values quoted correspond to the median value (i.e., 50% quantile) of each parameter. The results are also presented in the Figures 4–8 and 9–16, as one- and two-dimensional posterior probability density distributions. For each 1D probability density distributions, we determine the 68%, 90%, and 99% confidence regions using quantiles, which

TABLE 3
GLOBULAR CLUSTER RELEVANT PARAMETERS

Name	d_{GC} (kpc)	Method	$N_{H,22}$ (X-ray)	$N_{H,22}$ (HI)	Reference
M28	5.5 ± 0.3	Horizontal Branch fitting	$0.256^{+0.024}_{-0.024}$	0.24	Testa et al. (2001)
NGC 6397	2.02 ± 0.18	Dynamical	$0.096^{+0.017}_{-0.014}$	0.14	Rees (1996)
M13	6.5 ± 0.6	Dynamical	$0.008^{+0.044}_{-0.007}$	0.011	Rees (1996)
ω Cen	4.8 ± 0.3	Dynamical	$0.182^{+0.045}_{-0.042}$	0.09	van de Ven et al. (2006)
NGC 6304	6.22 ± 0.26	Horizontal Branch fitting	$0.346^{+0.105}_{-0.084}$	0.266	Recio-Blanco et al. (2005)

NOTE. — The selection of the distance values is described in Section 3.7, and the quoted uncertainties are 1σ . The N_H values are given in units of 10^{22} atoms cm^{-2} , with 90%-confidence uncertainties from X-ray spectral fitting. The N_H (HI) column corresponds to value in the direction of GCs, in the HI survey of (Dickey & Lockman 1990). The X-ray values are deduced from the best-fit N_H obtained from X-ray spectral fitting of each target in this work. Only the N_H values for NGC 6397 and ω Cen are not consistent with the HI values (see § 4.1 for details). N_H values deduced from the present X-ray spectral analysis are used in the present work.

are delimited by the solid, dashed and dotted lines in the 1D probability density distribution of each figure (Figures 4–8 and 9–16). This ensures that the integrated probabilities on each side of the median are equal (i.e., equal areas under the probability density curves). In addition, the median value of some parameters are different from the most probable value, especially in the case of highly skewed parameter posterior distributions. In some cases, the normalized probability of a parameter posterior distribution does not converge to zero within the parameter’s hard limits in *XSPEC*. This is indicated by a ‘p’ in the tables listing the parameters. The 2D posterior distributions are normalized to unity and the color bars indicate the probability density in each bin. The 68%, 90%, and 99% contours are obtained by calculating the lines of constant probability density that enclose 68%, 90%, and 99% of the accepted MCMC steps, respectively.

3.7. Distances to the Globular Clusters and their Uncertainties

While most GCs have distances estimated from photometry – using RR Lyrae variable stars (Marconi et al. 2003; Bono et al. 2007), horizontal branch stars (Valenti et al. 2007; Gratton et al. 2010), or the carbon-oxygen white-dwarf (CO-WD) sequence (Hansen et al. 2007) – these methods suffer from systematic uncertainties that are difficult to quantify. In fact, many recent photometric studies of GCs do not quote the amount of uncertainty in the measured distance (Rosenberg et al. 2000; Bica et al. 2006; Gratton et al. 2010).

While some references discuss systematic uncertainties related to the correction of extinction (e.g. McDonald et al. 2009, for ω Cen), other sources of systematic errors can affect the results, including errors related to the metallicity of cluster members (see dispersion in Figure 1 of Harris 2010), to a possible differential reddening in the direction of GCs (as observed for ω Cen, Law et al. 2003), to variations in the modeling of extinction with $R(V) \sim 3.1 - 3.6$ (adding $\sim 10\%$ of uncertainty, Grebel & Roberts 1995), or to the stellar evolution/atmosphere models used. As an example for the latter, distance determination methods to NGC 6397 using CO-WD may be affected by uncertainties in the evolutionary code models (Hansen et al. 2007; Strickler et al. 2009), which are not easily quantifiable.

Therefore, whenever possible, dynamical distance mea-

surements are used – distances estimated from proper motion and radial velocities of cluster members. These purely geometrical methods produce well-understood uncertainties, although they are at the moment larger than reported uncertainties from photometric methods. This is consistent with the goal of this paper which is to estimate R_{NS} and its uncertainties, minimizing systematic uncertainties. The upcoming mission GAIA from the European Space Agency, scheduled for 2013, is expected to produce GC distance measurements, to an accuracy of few percent, by determining the parallax of cluster members (Baumgardt & Kroupa 2005; Baumgardt 2008).

The adopted distance values are discussed below and are summarized in Table 3. In the following list, uncertainties are quoted at the 1σ level (for GC distances, distance moduli, etc.)

- The GC M28 does not have a dynamical distance measurement, but its distance has been estimated in different works: 5.1 ± 0.5 kpc (Rees & Cudworth 1991), $4.8 - 5.0$ kpc (Davidge et al. 1996) and 5.5 kpc (Harris 1996; Testa et al. 2001), all using photometric methods. For the most recent result, uncertainties can be estimated from the uncertainties in the horizontal branch (HB) magnitude. Specifically, the uncertainty in $V_{HB} = 15.55 \pm 0.1$, translates into the uncertainty in the distance: $d_{M28} = 5.5 \pm 0.3$ kpc (Servillat et al. 2012). This measured value and its uncertainties were used here.
- The distance to NGC 6397 has been reported from a dynamical study to be $d_{NGC\ 6397} = 2.02 \pm 0.18$ kpc (Rees 1996). More recent photometric studies (CO WD sequence) have been performed, with $d = 2.54 \pm 0.07$ kpc (Hansen et al. 2007), or $d = 2.34 \pm 0.13$ kpc (Strickler et al. 2009), but since those results are model-dependent, they are not used in an effort to minimize unquantified systematics. When the present analysis was at an advanced near-completion stage, recent results reporting a dynamical measurement of the distance came to our attention: $d_{NGC\ 6397} = 2.2^{+0.5}_{-0.7}$ kpc (Heyl et al. 2012), consistent with $d_{NGC\ 6397} = 2.02 \pm 0.18$ kpc, the value used in the present work.
- For M13, the dynamical distance has been measured: $d_{M13} = 6.5 \pm 0.6$ kpc (Rees 1996). No other

TABLE 4
SPECTRAL FIT RESULTS OF INDIVIDUAL SOURCES

Target	kT_{eff} (keV)	R_{NS} (km)	M_{NS} (M_{\odot})	R_{∞} (km)	$N_{H,22}$	$\chi^2_{\nu}/\text{d.o.f.}$ (prob.)
M28	120^{+44}_{-12}	$10.5^{+2.0}_{-2.9}$	$1.25^{+0.54}_{-0.63p}$	$13.0^{+2.3}_{-1.9}$	$0.252^{+0.025}_{-0.024}$	0.94 / 269 (0.76)
NGC 6397	76^{+14}_{-7}	$6.6^{+1.2}_{-1.1p}$	$0.84^{+0.30}_{-0.28p}$	$8.4^{+1.3}_{-1.1}$	$0.096^{+0.017}_{-0.015}$	1.06 / 223 (0.25)
M13	83^{+26}_{-11}	$10.1^{+2.8p}_{-3.7}$	$1.27^{+0.71}_{-0.63p}$	$12.8^{+4.7}_{-2.4}$	$0.008^{+0.044}_{-0.007p}$	0.94 / 63 (0.62)
ω Cen	64^{+17}_{-7}	$20.1^{+7.4p}_{-7.2}$	$1.78^{+1.03p}_{-1.07p}$	$23.6^{+7.6}_{-7.1}$	$0.182^{+0.041}_{-0.047}$	0.83 / 50 (0.80)
NGC 6304	107^{+32}_{-17}	$9.6^{+4.9}_{-3.4p}$	$1.16^{+0.90}_{-0.56p}$	$12.2^{+6.1}_{-3.8}$	$0.346^{+0.099}_{-0.093}$	1.07 / 29 (0.36)
M28	119^{+39}_{-9}	$10.6^{+0.9}_{-2.6}$	$1.17^{+0.51}_{-0.56p}$	$12.9^{+0.9}_{-0.9}$	(0.252)	0.94 / 270 (0.77)
NGC 6397	76^{+15}_{-6}	$6.6^{+0.7}_{-1.1p}$	$0.84^{+0.24}_{-0.28p}$	$8.4^{+0.5}_{-0.5}$	(0.096)	1.06 / 224 (0.26)
M13	86^{+27}_{-10}	$9.2^{+1.7}_{-2.3p}$	$1.15^{+0.42}_{-0.53p}$	$11.6^{+1.8}_{-1.5}$	(0.008)	0.93 / 64 (0.63)
ω Cen	64^{+13}_{-5}	$19.6^{+3.3}_{-3.8}$	$1.84^{+0.98p}_{-1.10p}$	$23.2^{+3.6}_{-3.3}$	(0.182)	0.82 / 51 (0.82)
NGC 6304	106^{+31}_{-13}	$9.4^{+2.4}_{-2.4p}$	$1.12^{+0.52}_{-0.51p}$	$11.8^{+2.5}_{-2.0}$	(0.346)	1.05 / 30 (0.39)

NOTE. — The targets were fit individually with fixed distances. The top part shows the results of fits obtained with free values of N_H , while the bottom shows results obtained with fixed N_H (indicated in parenthesis). For M28, the `pileup` model is included (see § 3.5 for details), and a value $\alpha = 0.45^{+0.13}_{-0.13}$ is obtained. The posterior distribution of R_{∞} was obtained by calculating the value of R_{∞} from R_{NS} and M_{NS} at each accepted MCMC iteration. Quoted uncertainties are 90% confidence. “p” indicates that the posterior distribution did not converge to zero probability within the hard limits of the model.

paper in the literature reports a distance measurement with quantified uncertainty. This dynamical measurement is consistent with the value $d_{\text{M13}} = 7.1$ kpc obtained from photometry (Harris 1996; Sandquist et al. 2010). While uncertainties could be estimated for this measurement like it was done for M28, the dynamical measurement is preferred to limit the effect of systematic uncertainties, as explained above.

- ω Cen’s distance was measured in a dynamical study, $d_{\omega \text{ Cen}} = 4.8 \pm 0.3$ kpc (van de Ven et al. 2006), and no other reference provides a distance with its measurement uncertainty. This measurement is consistent with other estimates (e.g. $d_{\omega \text{ Cen}} = 5.2$ kpc, Harris 1996, update 2010).
- The GC NGC 6304 lacks a dynamical distance measurement. However, results from a previous work (Recio-Blanco et al. 2005, using photometric data from Piotto et al. 2002) are available. In that work, the distance modulus in the F555W filter (*Hubble Space Telescope* filter) is $(m - M)_{F555W} = 15.58 \pm 0.09$. The reddening in this band for NGC 6304 was not provided in the published work, but the value $E(B - V) = 0.52$ (Piotto et al. 2002) can be used instead. This is acceptable because the average difference between $E(\text{HST})$ and $E(B - V)$ in the Recio-Blanco et al. (2005) catalogue is $\Delta E = 0.005$, which has a negligible effect on the absolute distance modulus. Therefore, $(m - M)_0 = 13.97 \pm 0.09$, assuming $A_V = 3.1 \times E(B - V)$, give $d_{\text{NGC 6304}} = 6.22 \pm 0.26$ kpc.

Overall, the distances to the targeted GCs have uncertainties of $\sim 9\%$ or less, keeping in mind that the distances determined with photometric methods possibly have systematically underestimated uncertainties.

4. RESULTS

In this section, the results of the spectral analyses of each target individually, with their R_{∞} measurements, are first presented. These include comparisons with previously published results. In particular, some issues regarding the reported spectral analyses for the qLMXBs in ω Cen and M13 are raised. Following this, the results of the R_{NS} measurement from the simultaneous fit are detailed.

4.1. R_{∞} Measurements of Individual qLMXBs

The analysis of the targeted qLMXBs is performed with the spectral model detailed above (§ 3.5). For each target, analyzed individually, the fits are statistically acceptable (i.e., with a null hypothesis probability larger than 1%), which demonstrates that, within the statistics of the observations, the sources did not experience any significant spectral variability over the time scale between the observations. The resulting values and 90% confidence uncertainties, along with the χ^2 -statistic obtained, are provided in Table 4. The spectral results obtained with N_H fixed at the X-ray-deduced values, instead of the usual HI survey values, are also provided. Discrepancies between the X-ray-deduced and HI survey values of N_H , if any, are discussed for each individual target.

Table 4 also shows the best-fit R_{∞} values, calculated using the equation:

$$R_{\infty} = R_{\text{NS}} \left(1 - \frac{2GM_{\text{NS}}}{R_{\text{NS}} c^2} \right)^{-1/2} \quad (3)$$

from each accepted points of the MCMC runs. Uncertainties in R_{∞} are then obtained from the calculated posterior distributions of R_{∞} resulting for the MCMC runs. The use of MCMC simulations has the advantage of avoiding geometrical construction to calculate the uncertainties of R_{∞} from the $M_{\text{NS}} - R_{\text{NS}}$ contours as performed in Guillot et al. (2011a).

In the following subsections, the previously published results are compared to those obtained here. To do so,

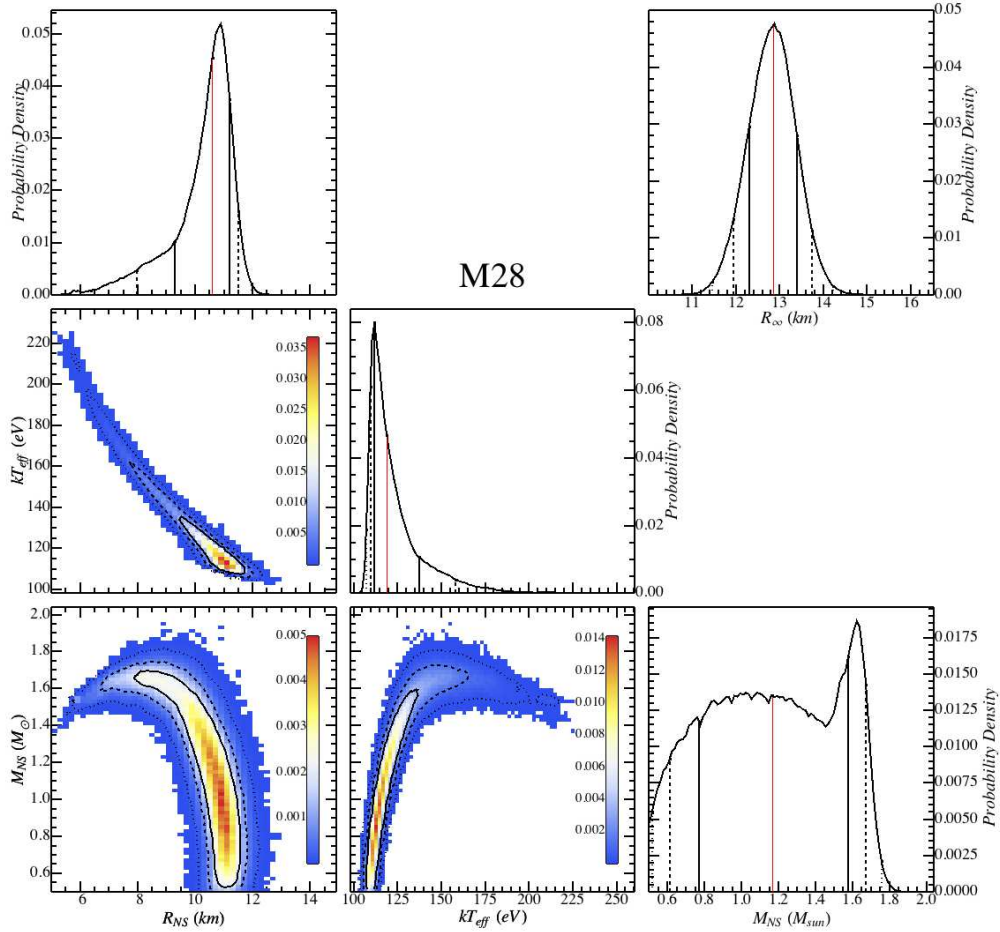


FIG. 4.— Figure showing the one- and two-dimensional marginalized posterior distributions for the NS properties (radius, temperature and mass) obtained from the MCMC run for the qLMXB in M28, for fixed distance and N_H , i.e., corresponding to the lower part of Table 4. The 1D and 2D posterior probability density distributions are normalized to unity. The top-right plot shows the 1D posterior distribution of R_∞ values. The 68%, 90% and 99% confidence intervals or regions are shown with solid, dashed, and dotted lines, respectively. In the 1D distributions, the median value is shown as a red line. Note that the 99% region is not always visible in the 1D distributions. The physical radius of the NS in M28 is $R_{NS} = 10.6^{+0.9}_{-2.6}$ km. This corresponds to a projected radius of $R_\infty = 12.9^{+0.9}_{-0.9}$ km, for $N_{H,22} = 0.252$. The double-peaked 1D distribution of M_{NS} is due to the strongly curved nature of the $M_{NS}-R_{NS}$ and $M_{NS}-kT_{\text{eff}}$ 2D distributions, i.e., the strong correlation between these parameters. The color scale in each 2D distribution represents the probability density in each bin. This figure and the following Figures 5–16 were created with the Mathematica package LevelSchemes (Caprio 2005).

the R_∞ measurements are renormalized to the distance used in the present analysis.

4.1.1. Comparison with Published Results - M28

Using the 2002 *Chandra* data, the reported R_∞ value of the qLMXB in M28 was $R_\infty = 14.5^{+6.9}_{-3.8}$ km ($D/5.5$ kpc) (Becker et al. 2003). An additional 200 ks of observations obtained with *Chandra*-ACIS in 2008 was used to produce a refined radius measurement: $R_{NS} = 9 \pm 3$ km and $M_{NS} = 1.4^{+0.4}_{-0.9} M_\odot$, with an H-atmosphere model (Servillat et al. 2012), corresponding to $R_\infty = 12.2^{+2.6}_{-1.4}$ km for $d_{M28} = 5.5$ kpc, consistent with the discovery work (Becker et al. 2003).

All the NS parameters resulting from the present analysis (Table 4, $R_\infty = 13.0^{+2.3}_{-1.9}$ km ($D/5.5$ kpc),

for $N_{H,22} = 0.252^{+0.025}_{-0.024}$) are also consistent with the previously published results. In addition, the previous work also performed a careful variability analysis (Servillat et al. 2012), confirming our findings that the qLMXB in M28 is not variable.

The best-fit N_H found here is consistent with the value from an HI survey: $N_{H,22} = 0.24$ (Dickey & Lockman 1990), but the X-ray-measured N_H value is preferred in the rest of the present work, for the MCMC runs with fixed N_H .

4.1.2. Comparison with Published Results - NGC 6397

The data sets used in this work are the same as the ones used in the previous work (Guillot et al. 2011a). There are however minor differences in the data reduction, namely, the extraction radius used (99% EEF in this

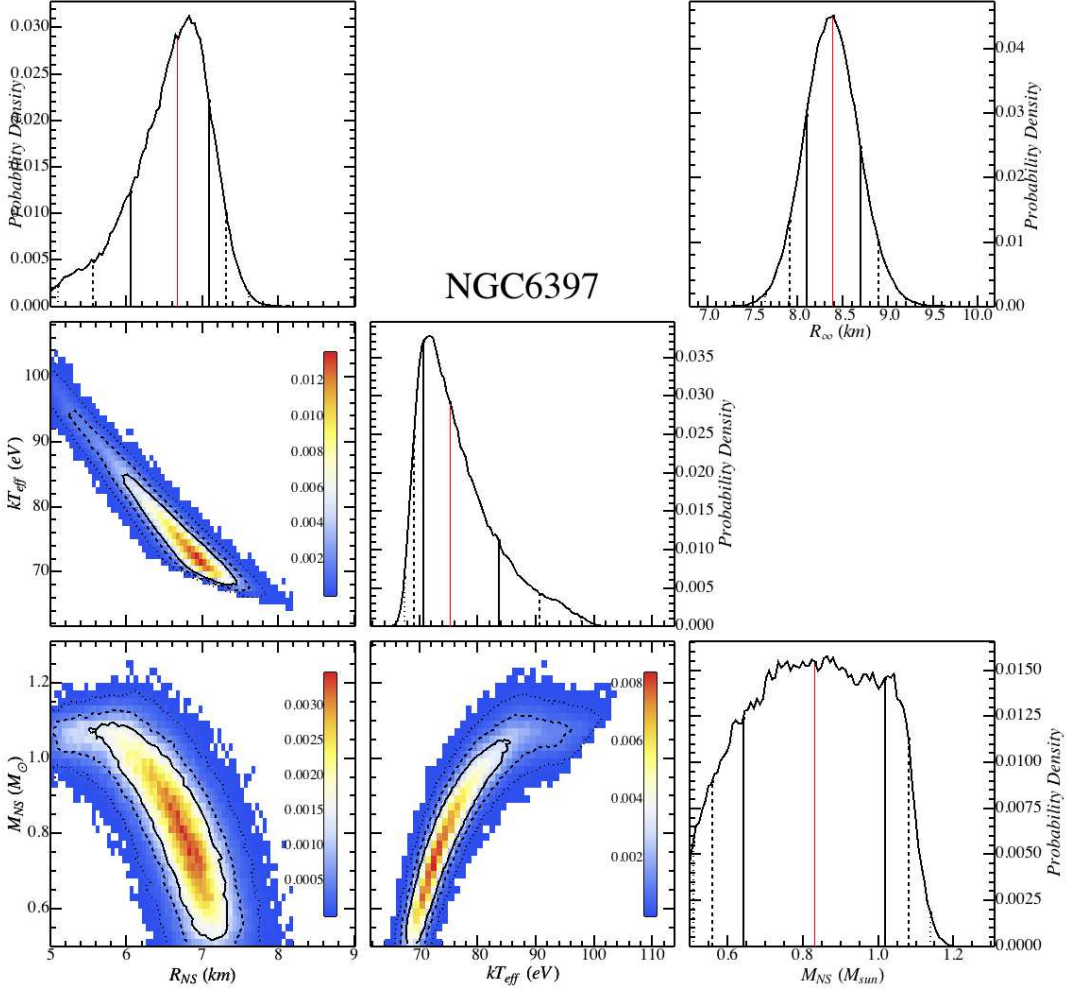


FIG. 5.— Figure similar to the precedent (Fig. 4), but for the qLMXB in NGC 6397. The physical radius of the NS is $R_{\text{NS}} = 6.6^{+0.7}_{-1.1p}$ km which corresponds to $R_{\infty} = 8.4^{+0.5}_{-0.5}$ km, for $N_{H,22} = 0.096$.

work compared to 98% EEf at 1 keV previously), the calibration files used (latest version of CALDB v4.4.8), the distance used for the spectral fit, and the energy range (0.5–8 keV in Guillot et al. 2011a).

After re-normalizing to the distance used in the present work, the previous R_{∞} result, $R_{\infty} = 9.6^{+0.8}_{-0.6}$ km ($D/2.02$ kpc), is consistent with the one obtained from the MCMC run: $R_{\infty} = 8.4^{+1.3}_{-1.1}$ km ($D/2.02$ kpc), for $N_{H,22} = 0.096^{+0.017}_{-0.015}$. This best-fit value of N_H is however, inconsistent with the fixed HI value ($N_H = 0.14$, Dickey & Lockman 1990) used in the previous work (Guillot et al. 2011a)¹². This puts into question the R_{NS} measurement and

¹² The X-ray deduced value of N_H found here is nonetheless consistent with the N_H value from a different survey of Galactic HI (Kalberla et al. 2005), $N_{H,22}=0.11$, and with the N_H value calculated from the reddening in the direction of NGC 6397 (Harris 1996) with a linear relation between N_H and the extinction A_V (Predehl & Schmitt 1995).

$M_{\text{NS}}-R_{\text{NS}}$ contours previously published with the value $N_{H,22}=0.14$ (Guillot et al. 2011a). When fixing $N_{H,22}=0.14$ in the present work, the resulting R_{∞} value is $R_{\infty} = 11.9^{+0.8}_{-0.8}$ km ($D/2.02$ kpc), marginally consistent with the (Guillot et al. 2011a) result. Nonetheless, one notices that the different value of N_H causes a significantly different resulting R_{NS} value. Basically, increasing the assumed value of N_H for a given target leads to a larger R_{∞} . This is further discussed in Section 5. In the rest of the present work, the best-fit X-ray deduced N_H value $N_{H,22} = 0.096$ is used.

4.1.3. Comparison with Published Results - ω Cen

The original R_{∞} measurement from the *Chandra* discovery observations was $R_{\infty} = 14.3 \pm 2.1$ km ($D/5.0$ kpc) for $N_{H,22} = 0.09$ (Rutledge et al. 2002), or $R_{\infty} = 13.7 \pm 2.0$ km ($D/4.8$ kpc). Another work measured $R_{\infty} = 13.6 \pm 0.3$ km ($D/5.3$ kpc) with $N_{H,22} = 0.09 \pm 0.025$, equivalent to $R_{\infty} = 12.3 \pm 0.3$ km ($D/4.8$ kpc),

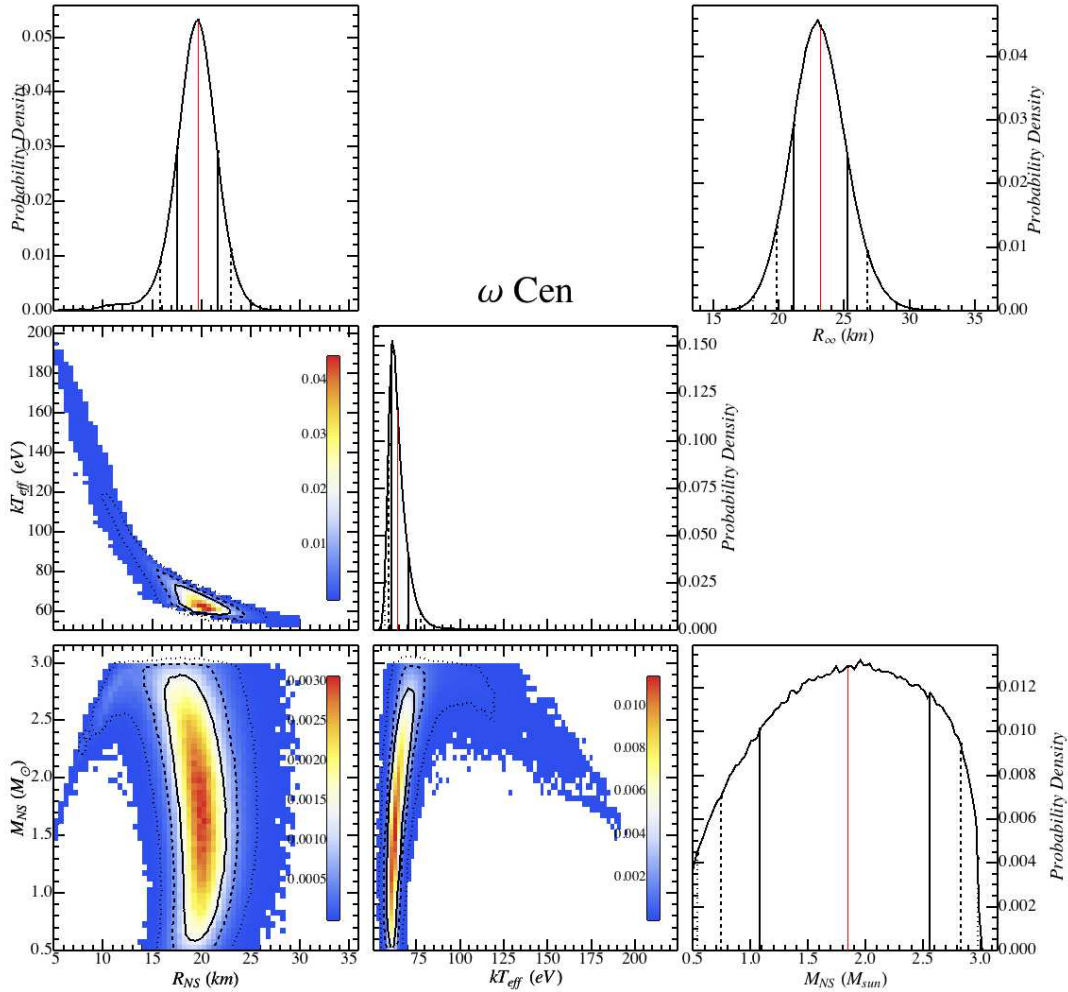


FIG. 6.— Figure similar to Fig. 4, but for the qLMXB in ω Cen. The physical radius of the NS is $R_{\text{NS}} = 19.6^{+3.3}_{-3.8}$ km which corresponds to $R_{\infty} = 23.2^{+3.6}_{-3.3}$ km, for $N_{H,22} = 0.182$.

using the *XMM* observation of ω Cen (Gendre et al. 2003a). Results from both analyses are consistent with the radius measurement performed in this work, with the value of Galactic absorption $N_{H,22}=0.09$: $R_{\infty} = 11.9^{+1.6}_{-1.4}$ km ($D/4.8$ kpc). However, when removing the constraint on N_H , the best-fit R_{∞} and N_H become inconsistent with the previously reported values. Specifically, $R_{\infty} = 23.6^{+7.6}_{-7.1}$ km ($D/4.8$ kpc) for $N_{H,22} = 0.182^{+0.041}_{-0.047}$. This value of N_H , not consistent with the HI survey value (Dickey & Lockman 1990), was used in the remainder of the present work. One can also note that the present results (best-fit R_{NS} , M_{NS} , kT_{eff} , and N_H) are consistent with those previously published (Webb & Barret 2007).

The results presented in Table 4 should be treated as more realistic than the initially reported one since they make use of more recent calibrations of *XMM* and *Chandra*, as well as an improved method. In particular, the small uncertainties ($\sim 2\%$) on R_{∞} previously

published (Gendre et al. 2003a) are particularly intriguing. It has also been shown in another reference that the S/N obtained with 50 ks exposure of ω Cen is not sufficient to constrain the radius with $\sim 2\%$ uncertainty (Webb & Barret 2007), but the cause of this discrepancy was not discussed. The constrained R_{NS} measurement with $\sim 2\%$ uncertainties (Gendre et al. 2003a) was not reproduced in the later work (Webb & Barret 2007, $R_{\text{NS}} = 11.7^{+7.0}_{-5.0}$ km, using the same *XMM* data), nor in the present work. Using the same model as the one initially used (Gendre et al. 2003a), similar uncertainties ($\sim 2\%$) can only be obtained when keeping the NS surface temperature fixed, leaving the normalization (i.e., the projected radius R_{∞}) as the sole free parameter. Specifically, with the same model and analysis procedure, the uncertainties on R_{∞} are $\sigma_{R_{\infty}} \sim 3\%$ with the temperature fixed and becomes $\sigma_{R_{\infty}} \sim 15\%$ when the temperature is a free parameter. If this is the

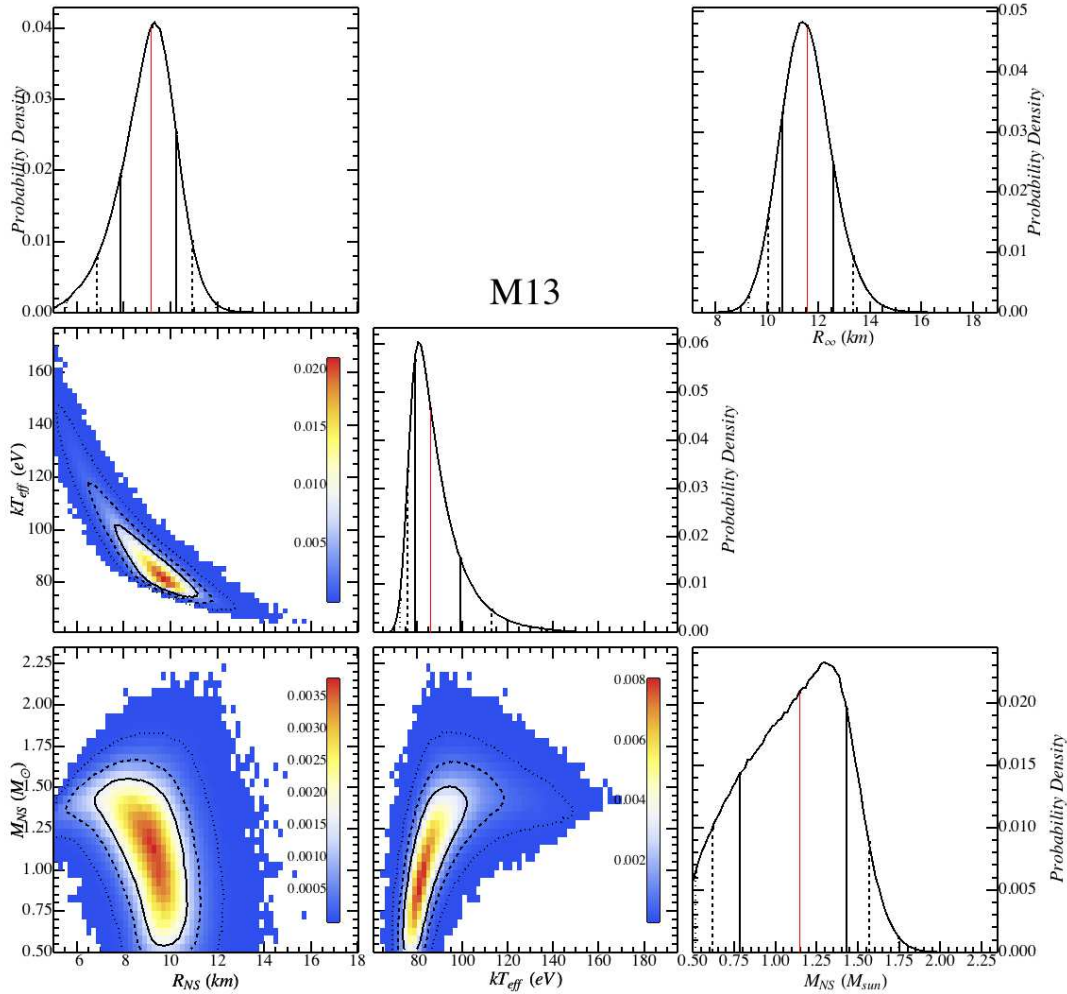


FIG. 7.— Figure similar to Fig. 4, but for the qLMBX in M13. The physical radius of the NS is $R_{\text{NS}} = 9.2^{+1.7}_{-2.3p}$ km which corresponds to $R_{\infty} = 11.6^{+1.8}_{-1.5}$ km, for $N_{H,22} = 0.008$.

method used in Gendre et al. (2003a), the uncertainties of R_{∞} only represent the statistical uncertainties and are therefore highly underestimated. It is inappropriate to keep the temperature fixed because there is no known prior on the NS surface temperature, and therefore it must remain free during the spectral fitting. In addition, the *XMM*-pn observations suffer from periods of high-background activity which need to be removed (see Figure 1). This leads to 34 ks of usable exposure time of the 41 ks available. No such background flares were reported in the original works (Gendre et al. 2003a; Webb & Barret 2007).

This note about the amount of uncertainty for ω Cen is of crucial importance since this source has often been cited as the canonical qLMBX, with the best radius measurement available, citing the underestimated $\sim 2\%$ uncertainties on R_{NS} . Deeper exposures of ω Cen are needed to provide constraints that will be useful for dEoS determination. Moreover, this discussion also points out

the importance of reporting $M_{\text{NS}}-R_{\text{NS}}$ contours (instead of simple R_{NS} measurements) for the measurements of NS properties using the thermal emission from qLMBXBs.

4.1.4. Comparison with Published Results - M13

The R_{∞} value of the qLMBX in M13 reported in the discovery paper (Gendre et al. 2003b), $R_{\infty} = 12.8 \pm 0.4$ km ($D/7.7$ kpc), corresponds to $R_{\infty} = 10.8 \pm 0.3$ km ($D/6.5$ kpc). This value is consistent with the value presented in the present work, given the uncertainties: $R_{\infty} = 12.8^{+4.7}_{-2.4}$ km ($D/6.5$ kpc), for $N_{H,22} = 0.008^{+0.044}_{-0.007p}$. The best fit N_H is consistent with HI survey values ($N_H = 0.011$, Dickey & Lockman 1990), but $N_{H,22} = 0.008$ is used in the remainder of the present analysis.

Once again, the uncertainties reported in the original work are small and can only be reproduced when fixing the temperature. Similarly to ω Cen, the M13 discovery

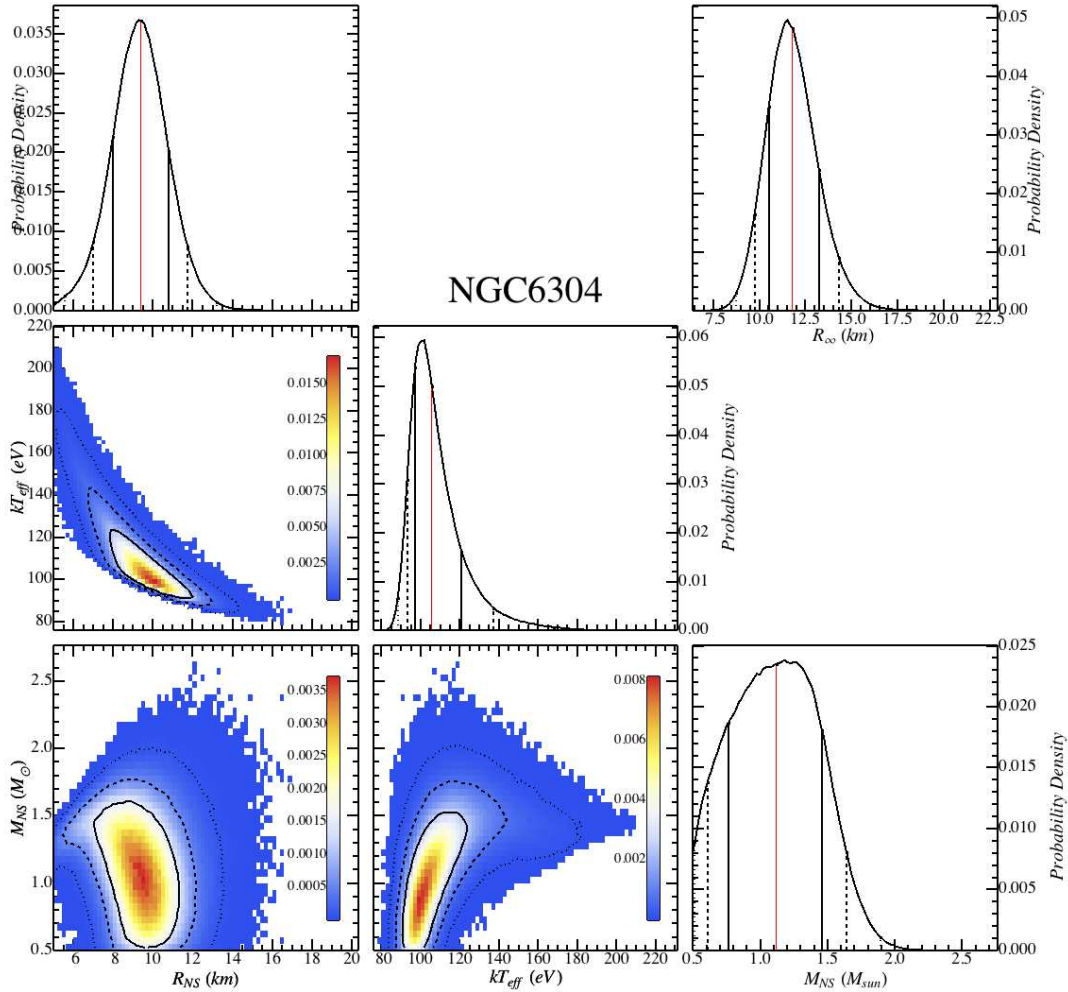


FIG. 8.— Figure similar to Fig. 4, but for the qLMXB in NGC 6304. The physical radius of the NS is $R_{\text{NS}} = 9.5^{+2.4}_{-2.0}$ km. The corresponding projected radius is $R_{\infty} = 11.8^{+2.5}_{-2.0}$ km, for $N_{\text{H},22} = 0.346$.

analysis was likely performed keeping the temperature frozen to estimate the uncertainty on the radius, and the ± 0.3 km uncertainties cited (Gendre et al. 2003b) are only systematic uncertainties.

In summary, the results found in this work for M13 are consistent with the existing ones (Gendre et al. 2003b; Webb & Barret 2007), and while our radius measurement uncertainties are not as constraining as those previously reported, they are considered more realistic given the S/N available for the observations, and given that more recent calibrations have been used. Similarly to ω Cen, deeper exposures of M13 would provide the necessary S/N to constrain the dEoS.

When the present work was at an advanced stage, results of a spectral analysis of the qLMXB in M13 came to our attention (Catuneanu et al. 2013). These results are consistent with those found in the present work, when re-normalized to the distance used here.

4.1.5. Comparison with published results - NGC 6304

This analysis presents a new 100 ks observation of NGC 6304. The R_{∞} value of the qLMXB, $R_{\infty} = 12.2^{+6.1}_{-3.8}$ km ($D/6.22$ kpc), for $N_{\text{H},22} = 0.346^{+0.099}_{-0.093}$, is consistent with that obtained from the *XMM* observation (Guillot et al. 2009a), $R_{\infty} = 12.1^{+6.6}_{-4.8}$ km ($D/6.22$ kpc), and with that from a short *Chandra* observation (Guillot et al. 2009b), $R_{\infty} = 7.8^{+8.6}_{-3.8}$ km ($D/6.22$ kpc), after re-normalizing the 2009 measurement to the distance used in the present paper. The best-fit X-ray deduced value is also consistent with the value used in the original work, obtained from HI surveys. Nonetheless, the X-ray measured N_{H} value is used in the remainder of the present work.

4.2. R_{NS} , Measurement of the Radius of Neutron Stars

In this section, the results of the simultaneous spectral fits with the parameter posterior distributions obtained

TABLE 5
RESULTS FROM SIMULTANEOUS SPECTRAL FITTING, WITH FIXED N_H

Target	α_{pileup}	kT_{eff} (eV)	M_{NS} (M_{\odot})	R_{∞} (km)	$N_{H,22}$	PL Norm $\times 10^{-7}$ $\text{keV}^{-1} \text{s}^{-1} \text{cm}^{-2}$
Run #1: Fixed N_H , Fixed d_{GC} , No PL included, $R_{\text{NS}}=7.1_{-0.6}^{+0.5}$ km						
χ^2_{ν}/dof (prob.) = 0.97/643 (0.70), 18% accept. rate						
M28	$0.44_{-0.11}^{+0.11}$	176_{-11}^{+14}	$1.62_{-0.08}^{+0.08}$	$12.5_{-0.6}^{+0.6}$	(0.252)	–
NGC 6397	–	71_{-3}^{+7}	$0.69_{-0.16p}^{+0.26}$	$8.4_{-0.5}^{+0.5}$	(0.096)	–
M13	–	110_{-10}^{+12}	$1.41_{-0.29}^{+0.21}$	$11.0_{-1.3}^{+1.4}$	(0.008)	–
ω Cen	–	164_{-14}^{+14}	$2.05_{-0.15}^{+0.13}$	$18.9_{-1.7}^{+1.7}$	(0.182)	–
NGC 6304	–	136_{-17}^{+18}	$1.41_{-0.43p}^{+0.25}$	$11.0_{-1.8}^{+1.8}$	(0.346)	–
Run #2: Fixed N_H , Gaussian Bayesian priors for d_{GC} , No PL included, $R_{\text{NS}}=7.6_{-0.9}^{+0.9}$ km						
χ^2_{ν}/dof (prob.) = 0.98/638 (0.64), 11% accept. rate						
M28	$0.44_{-0.10}^{+0.11}$	165_{-20}^{+22}	$1.63_{-0.15}^{+0.14}$	$12.6_{-1.0}^{+1.1}$	(0.252)	–
NGC 6397	–	71_{-3}^{+8}	$0.73_{-0.20p}^{+0.33}$	$9.0_{-0.9}^{+1.1}$	(0.096)	–
M13	–	101_{-16}^{+20}	$1.34_{-0.53p}^{+0.33}$	$11.0_{-1.7}^{+1.9}$	(0.008)	–
ω Cen	–	154_{-22}^{+21}	$2.16_{-0.21}^{+0.22}$	$19.3_{-2.1}^{+2.3}$	(0.182)	–
NGC 6304	–	127_{-19}^{+23}	$1.36_{-0.59p}^{+0.34}$	$11.0_{-1.8}^{+2.1}$	(0.346)	–
Run #3: Fixed N_H , Fixed d_{GC} , PL included, $R_{\text{NS}}=7.3_{-0.6}^{+0.5}$ km						
χ^2_{ν}/dof (prob.) = 0.96/638 (0.78), 15% accept. rate						
M28	$0.35_{-0.12}^{+0.12}$	170_{-11}^{+14}	$1.63_{-0.08}^{+0.08}$	$12.6_{-0.6}^{+0.6}$	(0.252)	$5.1_{-3.4p}^{+3.7}$
NGC 6397	–	70_{-3}^{+7}	$0.68_{-0.15p}^{+0.28}$	$8.6_{-0.5}^{+0.5}$	(0.096)	$2.2_{-1.3p}^{+1.3}$
M13	–	109_{-11}^{+12}	$1.50_{-0.32}^{+0.24}$	$11.7_{-1.5}^{+1.8}$	(0.008)	$2.2_{-2.0p}^{+4.2}$
ω Cen	–	163_{-14}^{+13}	$2.14_{-0.16}^{+0.14}$	$19.9_{-1.9}^{+1.9}$	(0.182)	$2.9_{-2.4p}^{+3.7}$
NGC 6304	–	136_{-17}^{+18}	$1.51_{-0.44p}^{+0.26}$	$11.7_{-2.0}^{+2.0}$	(0.346)	$1.7_{-1.5p}^{+2.5}$
Run #4: Fixed N_H , Gaussian Bayesian priors for d_{GC} , PL included, $R_{\text{NS}}=8.0_{-1.0}^{+1.0}$ km						
χ^2_{ν}/dof (prob.) = 0.97/633 (0.72), 11% accept. rate						
M28	$0.35_{-0.12}^{+0.12}$	157_{-20}^{+24}	$1.64_{-0.18}^{+0.15}$	$12.8_{-1.0}^{+1.0}$	(0.252)	$5.0_{-3.4p}^{+3.8}$
NGC 6397	–	70_{-3}^{+8}	$0.72_{-0.19p}^{+0.37}$	$9.4_{-1.0}^{+1.1}$	(0.096)	$2.2_{-1.3p}^{+1.3}$
M13	–	99_{-17}^{+22}	$1.43_{-0.61p}^{+0.37}$	$11.7_{-1.9}^{+2.3}$	(0.008)	$2.2_{-1.9p}^{+4.0}$
ω Cen	–	151_{-21}^{+21}	$2.28_{-0.25}^{+0.25}$	$20.4_{-2.4}^{+2.6}$	(0.182)	$3.0_{-2.5p}^{+3.8}$
NGC 6304	–	125_{-20}^{+24}	$1.46_{-0.69p}^{+0.36}$	$11.8_{-2.1}^{+2.2}$	(0.346)	$1.7_{-1.5p}^{+2.4}$

NOTE. — α_{pileup} corresponds to the parameter of the pileup model. “PL Norm.” refers to the value of the normalization of the power-law component, when used. For each run, the characteristics are described: whether or not the absorption N_H was fixed; whether the GC distances d_{GC} were fixed or if a Bayesian prior was imposed; whether or not a additional power-law component (PL) was included in the model. For each run, the best χ^2_{ν} value is provided, as well as the null hypothesis probability. Finally, the acceptance rate (not including the burn-in period) is provided. All quoted uncertainties are 90% confidence. Values in parentheses are kept fixed in the analysis. “p” indicates that the posterior distribution did not converge to zero probability within the hard limit of the model.

from the MCMC simulations are presented. The following distinct MCMC runs are performed:

- Run #1: Model `nsatmos` with fixed N_H values and fixed distances: 12 free parameters, 25 Stretch-Move walkers.
- Run #2: Model `nsatmos` with fixed N_H values and Gaussian Bayesian priors for the distances: 17 free parameters, 30 Stretch-Move walkers.
- Run #3: Model `nsatmos` with fixed N_H values and fixed distances, and an additional PL component: 17 free parameters, 30 Stretch-Move walkers.
- Run #4: Model `nsatmos` with fixed N_H values, Gaussian Bayesian priors for the distances, and an additional PL component (with fixed index $\Gamma = 1.0$, but free normalizations): 22 free parameters, 35 Stretch-Move walkers.
- Run #5: Model `nsatmos` with free N_H values and fixed distances: 17 free parameters, 30 Stretch-Move walkers.
- Run #6: Model `nsatmos` with free N_H values and Gaussian Bayesian priors for the distances: 22 free parameters, 35 Stretch-Move walkers.
- Run #7: Model `nsatmos` with free N_H values, Gaussian Bayesian priors for the distances, and an additional PL component: 27 free parameters, 40 Stretch-Move walkers. The spectra resulting from this run are shown in Figure 3.
- Run #8: Model `nsaggrav` with fixed N_H values and fixed distances: 12 free parameters, 25 Stretch-Move walkers. This model is used for comparison with the `nsatmos` model.

All the runs converged to a statistically acceptable point in the parameter space, with $\chi^2_{\nu} \sim 1$ and a null hypoth-

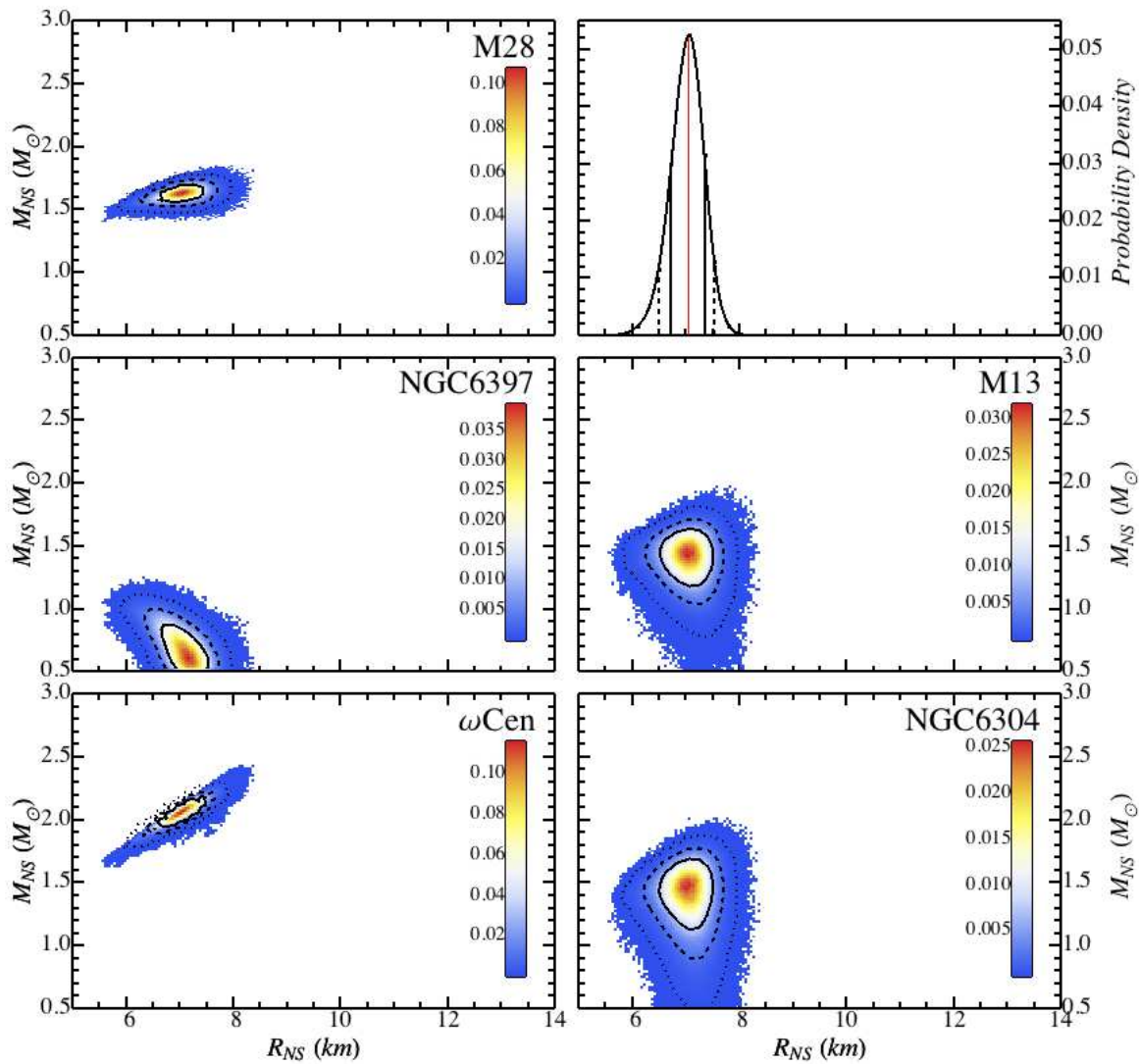


FIG. 9.— Figure showing the marginalized posterior distribution in $M_{\text{NS}}-R_{\text{NS}}$ space for the five qLMXBs, in the first MCMC run, where the distance and the hydrogen column density N_H are fixed and where no PL component is added, corresponding to Run #1. The 1D and 2D posterior probability distributions are normalized to unity. The color scale in the 2D distributions represents the probability density in each bin. The 68%, 90% and 99%-confidence contours are shown with solid, dashed and dotted lines on the $M_{\text{NS}}-R_{\text{NS}}$ density plots, respectively. The top-right graph is the resulting normalized probability distribution of R_{NS} , common to the five qLMXBs, with the 68%, 90% and 99%-confidence regions represented by the solid, dashed and dotted vertical lines. The median value is shown by the red line. The measured radius is $R_{\text{NS}} = 7.1^{+0.5}_{-0.6}$ km (90% confidence).

esis probability > 0.01 . In addition, the acceptance rate of each run is large enough ($> 5\%$) that the model used and the assumptions are adequate for the data. From the accepted steps of each run, the marginalized posterior distributions of all parameters and the median values with 90% confidence regions are quoted in the tables. In addition, $M_{\text{NS}}-R_{\text{NS}}$ posterior distributions for each of the five qLMXBs are obtained.

Run #1 was performed with the maximum constraints imposed on the model. With the assumptions imposed on the parameters, this run leads to the most constrained $M_{\text{NS}}-R_{\text{NS}}$ contours of this work, resulting in $R_{\text{NS}} = 7.1^{+0.5}_{-0.6}$ km (90%-confidence), and the minimum

χ^2_{ν}/dof (prob.) = 0.97/643 (0.70). Detailed information for other parameters is shown in Table 5.

The possible effect of auto-correlation between the steps of the MCMC simulation is investigated by selecting every other 10 accepted point, a method called thinning (MacEachern & Berliner 1994). The resulting confidence regions for all parameters are not affected by thinning and it can be safely concluded that the steps in the MCMC runs are not subject to auto-correlation. All the accepted steps of each run are therefore used to create the posterior distributions.

Following the first run, all assumptions (on distance, N_H and the presence of a PL) are progressively relaxed in the MCMC Runs #2 through #7, with the last one

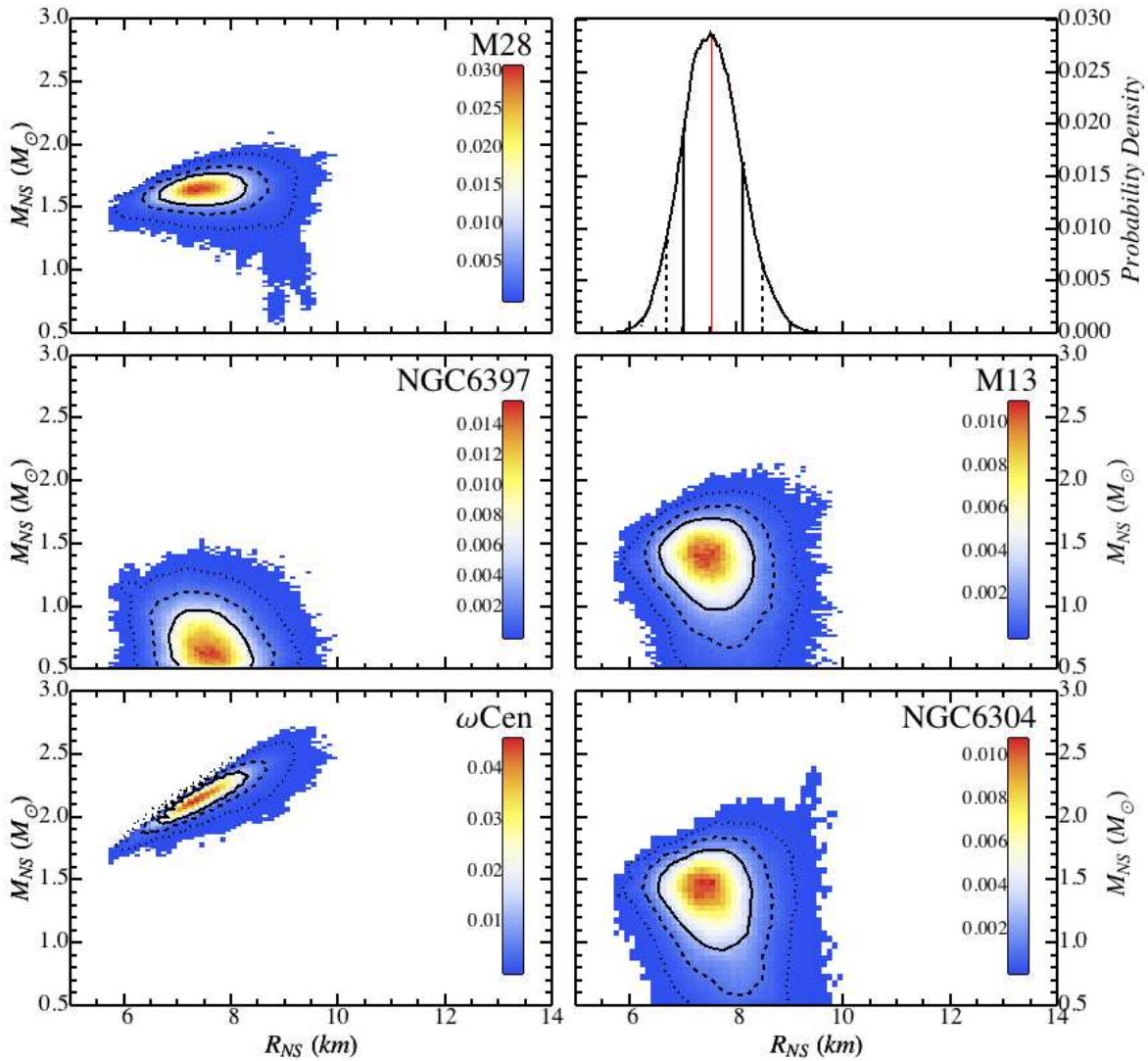


FIG. 10.— Figure similar to the previous one, Fig 9, but for the MCMC Run #2, where Gaussian Bayesian priors were used for the distances to the five qLMXBs (see Table 3). The resulting radius measurement is $R_{\text{NS}} = 7.6_{-0.9}^{+0.9}$ km.

producing the R_{NS} measurement with the fewest assumptions. The $M_{\text{NS}}-R_{\text{NS}}$ contours and R_{NS} distribution of each of these are displayed in Figures 9–15 and the results are listed in Tables 5 and 6. In the process of relaxing assumptions, one confirms that the results remain consistent between each run and such process does not significantly bias the results. The effects of relaxing each assumption are briefly described below.

4.2.1. Using Gaussian Bayesian Priors for Distances

When adding Gaussian Bayesian priors in place of the fixed distance parameters, the $M_{\text{NS}}-R_{\text{NS}}$ contours are, as expected, broader in the R_{∞} direction. Because the normalization of a thermal spectrum such as `nsatmos` is $\propto (R_{\infty}/d)^2$, relaxing the assumptions on d_{GC} increases the possible values of R_{∞} . This effect is mostly noticeable for the two targets observed with the highest S/N, i.e., M28 and NGC 6397. In Run #2, the posterior distribution

of R_{NS} corresponds to $R_{\text{NS}} = 7.6_{-0.9}^{+0.9}$ km, broader than that of the previous run.

4.2.2. Adding a Power-Law Spectral Component

When adding PL components to account for possible excesses of photons at high energy, one finds NS parameters consistent with those of the previous runs. Most PL normalizations are consistent with zero in Runs #3, #4 and #7. For M28, the PL normalizations in these runs is consistent with zero, within 2.4σ . For NGC 6397 in Runs #3 and #4, the consistency with zero is only marginal, within 2.8σ . Finally, in Run #7, the PL normalization of NGC 6397, $\text{Norm}_{\text{PL,NGC 6397}} = 2.7_{-1.3}^{+1.3} \times 10^{-7} \text{ keV}^{-1} \text{ s}^{-1} \text{ cm}^{-2}$, is not consistent with zero. This may indicate the possible contribution of a PL component at large energies and it is further discussed in Section 5.

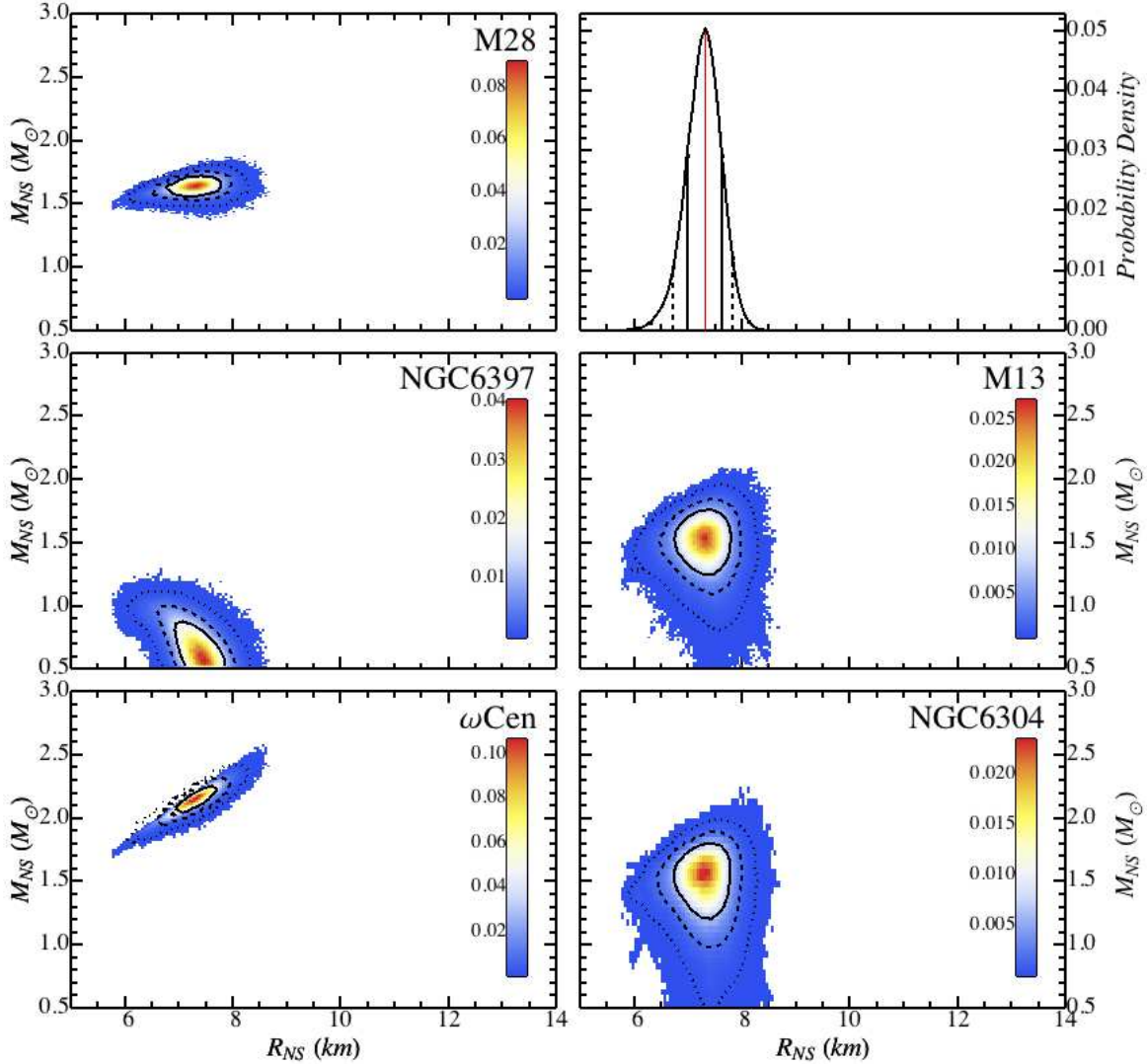


FIG. 11.— Figure similar to Figure 9, corresponding to the results of Run #3. In this run, the distances are fixed (no priors included), but a PL component (with fixed index $\Gamma = 1$) is added to the spectral model, leading to $R_{\text{NS}} = 7.3^{+0.5}_{-0.6}$ km.

4.2.3. Relaxing the N_H assumption

As the constraints on the N_H parameters are relaxed, the `nsatmos` best-fit parameters remain consistent with those of the previous runs. The posterior distributions of the five N_H parameters are consistent with the X-ray deduced N_H values found from the spectral fits of the sources individually, i.e., the values used in Run #1–4.

4.2.4. All Assumptions Relaxed

For this final run (#7), $R_{\text{NS}} = 9.1^{+1.3}_{-1.5}$ km is consistent with the radii obtained in the previous MCMC runs (#1–6). The posterior distributions of $M_{\text{NS}}-R_{\text{NS}}$ are shown in Figure 15 and detailed in Table 6. Once again, all resulting values are consistent with those of the previous runs. Progressively relaxing assumptions ensures a good understanding of the spectral fit, with no unexpected behavior.

4.2.5. Comparison with `nsagrav`

We also performed the fit using the model `nsagrav` instead of `nsatmos` for comparison purposes. It has previously been shown that `nsatmos` and `nsagrav` produce similar spectral parameters when fit to experimental data (e.g. Webb & Barret 2007). In `XSPEC`, for the `nsagrav` model, the R_{NS} range is [6 km, 20 km], and the M_{NS} range is [$0.3 M_{\odot}$, $2.5 M_{\odot}$] compared to [5 km, 30 km] and [$0.5 M_{\odot}$, $3.0 M_{\odot}$] with `nsatmos`. This run (#8) was done with the same characteristics as Run #1.

When comparing the posterior distributions of the parameters and $M_{\text{NS}}-R_{\text{NS}}$ contours obtained with `nsagrav` (Figure 16 for Run #1 and Table 7) to those obtained with `nsatmos` (Figure 9 and Table 5), some consistencies can be noticed. However, not all distributions are consistent between the two models. Specifically, for M28, M13, and NGC 6304, one can notice that an additional distinct

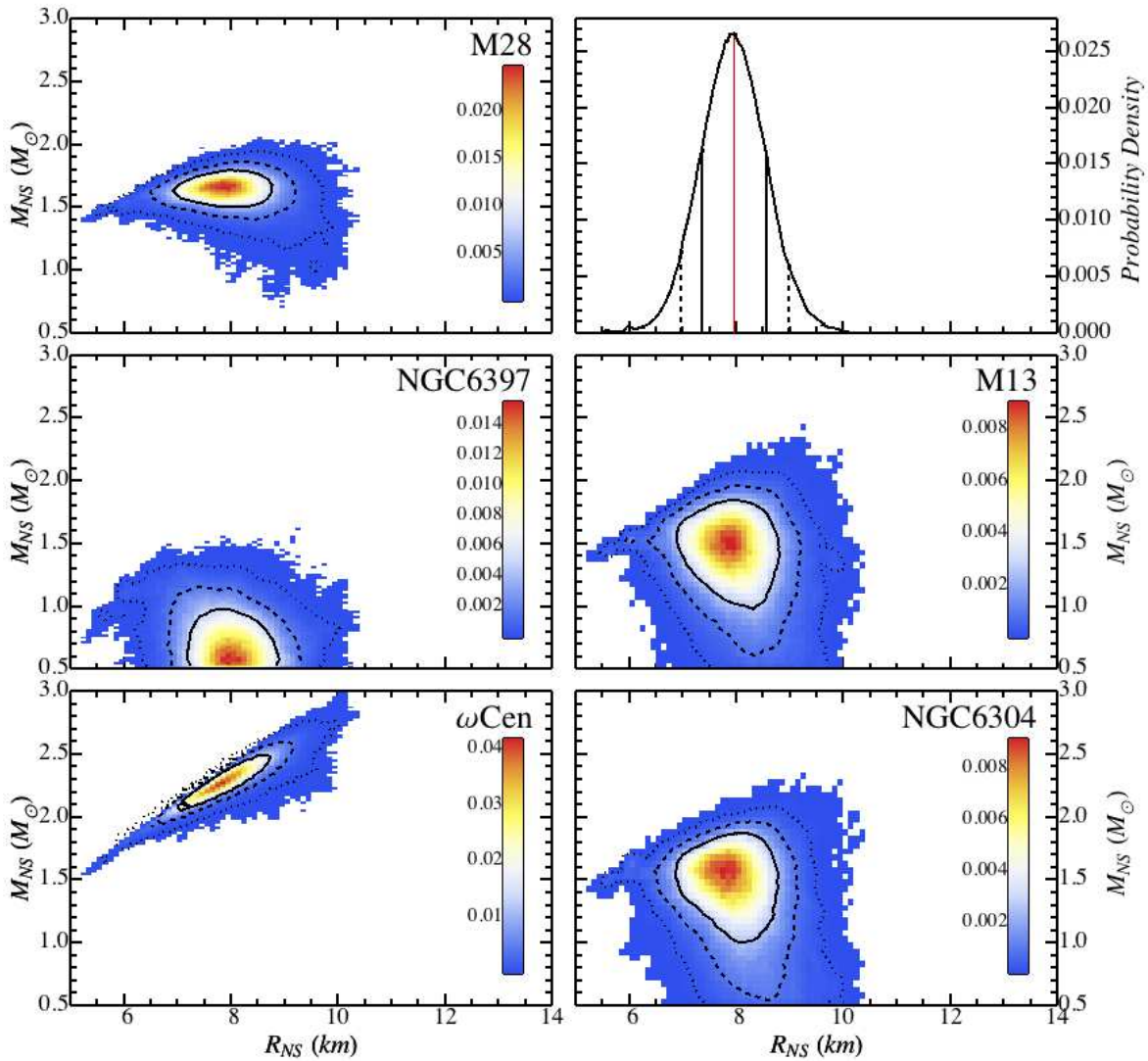


FIG. 12.— Figure similar to Figure 9, but for Run #4. Here, the Gaussian Bayesian priors on the distances are included, as well as the PL spectral component, with N_H held fixed. The resulting NS radius is $R_{\text{NS}} = 8.0^{+1.0}_{-1.0}$ km.

lobe at high M_{NS} appears in the $M_{\text{NS}}-R_{\text{NS}}$ parameter space. This appears to be because the `nsaggrav` model as implemented in `XSPEC` gives different values in this parameter space than returned by `nsatmos`; the authors of this model state that this is because the model is inapplicable in this parameter region¹³ (Zavlin and Pavlov, priv. comm.). For example, some sets of $M_{\text{NS}}-R_{\text{NS}}$ allowed by `nsaggrav` and giving an acceptable χ^2 -value lead to imaginary values of R_{∞} . It is important for an observer to keep this fact in mind, otherwise, results produced by the `XSPEC` implementation of `nsaggrav` could be misinterpreted. In light of the pitfall mentioned here, the `nsaggrav` model should be used with care.

¹³ The $M_{\text{NS}}-R_{\text{NS}}$ space where `nsaggrav` is applicable can be seen here <http://heasarc.gsfc.nasa.gov/xanadu/xspec/models/m-r.pdf>

5. DISCUSSION

This paper presented the simultaneous analysis of the spectra from five qLMXBs in GCs with a common R_{NS} parameter for all targets. The posterior distributions for R_{NS} , M_{NS} , R_{∞} , kT_{eff} , and N_H were obtained from MCMC simulations, which included Gaussian Bayesian priors for the distances to the GCs hosting the targets. In this discussion section, the original work performed here and the data used are summarized. This is followed by a subsection discussing various possible biases resulting from the MCMC analysis. The discussion finishes with the implication that the resulting R_{NS} measurement may have for the determination of the dEoS.

5.1. List of New Analysis Methods, Data and Results

The following two paragraphs aim at summarizing the novel approach to the analysis of the NS thermal spec-

TABLE 6
RESULTS FROM THE SIMULTANEOUS SPECTRAL FITTING, WITH FREE N_H

Target	α_{pileup}	kT_{eff} (eV)	M_{NS} (M_{\odot})	R_{∞} (km)	$N_{H,22}$	PL Norm $\times 10^{-7}$ $\text{keV}^{-1} \text{s}^{-1} \text{cm}^{-2}$
Run #5: Free N_H , Fixed d_{GC} , No PL included, $R_{\text{NS}}=7.5^{+1.1}_{-1.0}$ km						
χ^2_{ν}/dof (prob.) = 0.98/638 (0.66), 8% accept. rate						
M28	$0.43^{+0.13}_{-0.13}$	165^{+24}_{-22}	$1.60^{+0.21}_{-0.25}$	$12.4^{+1.6}_{-1.5}$	$0.248^{+0.023}_{-0.022}$	—
NGC 6397	—	70^{+8}_{-5}	$0.76^{+0.33}_{-0.22p}$	$9.0^{+1.4}_{-1.1}$	$0.105^{+0.016}_{-0.015}$	—
M13	—	106^{+20}_{-16}	$1.43^{+0.36}_{-0.44p}$	$11.4^{+2.5}_{-1.7}$	$0.010^{+0.024}_{-0.009p}$	—
ω Cen	—	137^{+32}_{-31}	$2.00^{+0.36}_{-0.41}$	$16.7^{+4.7}_{-4.3}$	$0.152^{+0.048}_{-0.049}$	—
NGC 6304	—	120^{+28}_{-14}	$1.13^{+0.59}_{-0.54p}$	$10.1^{+3.2}_{-1.9}$	$0.315^{+0.079}_{-0.060}$	—
Run #6: Free N_H , Gaussian Bayesian priors for d_{GC} , No PL included, $R_{\text{NS}}=7.8^{+1.3}_{-1.1}$ km						
χ^2_{ν}/dof (prob.) = 0.99/633 (0.59), 8% accept. rate						
M28	$0.42^{+0.13}_{-0.13}$	158^{+26}_{-29}	$1.59^{+0.25}_{-0.45p}$	$12.4^{+1.8}_{-1.7}$	$0.248^{+0.023}_{-0.022}$	—
NGC 6397	—	71^{+9}_{-5}	$0.78^{+0.39}_{-0.24p}$	$9.4^{+1.6}_{-1.3}$	$0.104^{+0.016}_{-0.015}$	—
M13	—	100^{+23}_{-18}	$1.38^{+0.42}_{-0.64p}$	$11.3^{+2.6}_{-2.0}$	$0.010^{+0.023}_{-0.009p}$	—
ω Cen	—	133^{+35}_{-30}	$2.07^{+0.41p}_{-0.43}$	$17.1^{+5.2}_{-4.4}$	$0.156^{+0.050}_{-0.048}$	—
NGC 6304	—	116^{+30}_{-14}	$1.09^{+0.68}_{-0.52p}$	$10.3^{+3.4}_{-1.9}$	$0.321^{+0.078}_{-0.061}$	—
Run #7: Free N_H , Gaussian Bayesian priors for d_{GC} , PL included, $R_{\text{NS}}=9.1^{+1.3}_{-1.5}$ km						
χ^2_{ν}/dof (prob.) = 0.98/628 (0.64), 7% accept. rate						
M28	$0.34^{+0.14}_{-0.14}$	137^{+29}_{-22}	$1.50^{+0.37}_{-0.80p}$	$12.6^{+2.0}_{-2.0}$	$0.248^{+0.024}_{-0.023}$	$5.0^{+3.7}_{-3.4p}$
NGC 6397	—	67^{+8}_{-5}	$0.86^{+0.47}_{-0.31p}$	$10.8^{+1.7}_{-1.7}$	$0.116^{+0.017}_{-0.017}$	$2.7^{+1.3}_{-1.3}$
M13	—	92^{+24}_{-15}	$1.47^{+0.62}_{-0.78p}$	$12.6^{+3.7}_{-2.3}$	$0.014^{+0.028}_{-0.012p}$	$2.4^{+4.1}_{-2.1p}$
ω Cen	—	130^{+33}_{-31}	$2.42^{+0.42p}_{-0.54}$	$20.3^{+5.6}_{-5.7}$	$0.172^{+0.047}_{-0.051}$	$2.9^{+3.9}_{-2.6p}$
NGC 6304	—	112^{+31}_{-15}	$1.32^{+0.80}_{-0.71p}$	$12.1^{+4.3}_{-2.5}$	$0.346^{+0.086}_{-0.065}$	$1.8^{+2.6}_{-1.5p}$

NOTE. — This table is similar to Table 5, abbreviations and symbols are the same. The only difference is that the absorption N_H remained free for these runs. Quoted uncertainties are 90% confidence as well. “p” indicates that the posterior distribution did not converge to zero probability within the hard limit of the model.

TABLE 7
RESULTS FROM SIMULTANEOUS SPECTRAL FITTING WITH **nsagrav**

Target	α_{pileup}	kT_{eff} (eV)	M_{NS} (M_{\odot})	R_{∞} (km)	$N_{H,22}$	PL Norm $\times 10^{-7}$ $\text{keV}^{-1} \text{s}^{-1} \text{cm}^{-2}$
Run #8: Fixed N_H , Fixed d_{GC} , No PL included, $R_{\text{NS}}=7.8^{+0.5}_{-0.3}$ km						
χ^2_{ν}/dof (prob.) = 1.04/643 (0.25), 10% accept. rate						
M28	$0.46^{+0.11}_{-0.11}$	166^{+4}_{-13}	$2.03^{+0.42p}_{-0.43}$	$16.3^{+12.6}_{-3.9}$	(0.252)	—
NGC 6397	—	66^{+2}_{-2}	$0.51^{+0.23}_{-0.15p}$	$8.7^{+0.6}_{-0.5}$	(0.096)	—
M13	—	101^{+12}_{-11}	$1.42^{+0.88p}_{-0.49p}$	$11.5^{+11.2}_{-1.7}$	(0.008)	—
ω Cen	—	113^{+2}_{-3}	$1.86^{+0.36p}_{-0.15}$	$14.3^{+4.8}_{-1.2}$	(0.182)	—
NGC 6304	—	126^{+17}_{-19}	$1.41^{+0.97p}_{-0.74p}$	$11.4^{+14.1}_{-2.3}$	(0.346)	—

NOTE. — This table is similar to Table 5. But this run was performed with the **nsagrav** model instead of the **nsatmos** model for comparison purposes. The differences between the two models are described in Section 4.2, for example, in the high-redshift regime (See Figure 16). “p” indicates that the posterior distribution did not converge to zero probability within the hard limit of the model. Quoted uncertainties are 90% confidence.

tra, and unused data presented in this paper. The MCMC framework for spectral analysis is a rather recent approach, made convenient by the development of *PyXSPEC*, the Python version of *XSPEC*. The “Stretch-Move” MCMC algorithm used here differs from the usual Metropolis-Hasting (M-H) algorithm of standard MCMC simulations. It has been developed recently and while it presents significant advantages over M-H, it is still scarcely used in astrophysics. This work includes X-ray data not previously presented in the literature, namely the *Chandra* exposure of NGC 6304.

This paper also contains a more complete presentation of the resulting best-fit NSs physical parameters (kT_{eff} , M_{NS} , and R_{NS}). Specifically, the products of the MCMC simulations in 2-dimensional matrices of posterior distributions (see Figures 4–8) are displayed. Such figures better represent the true distributions of the NS physical parameters compared to simple lists of best-fit values with their uncertainties, mostly because the distribution are not necessarily Gaussian (particularly with models like **nsatmos**). We encourage researchers to present their results in such a way.

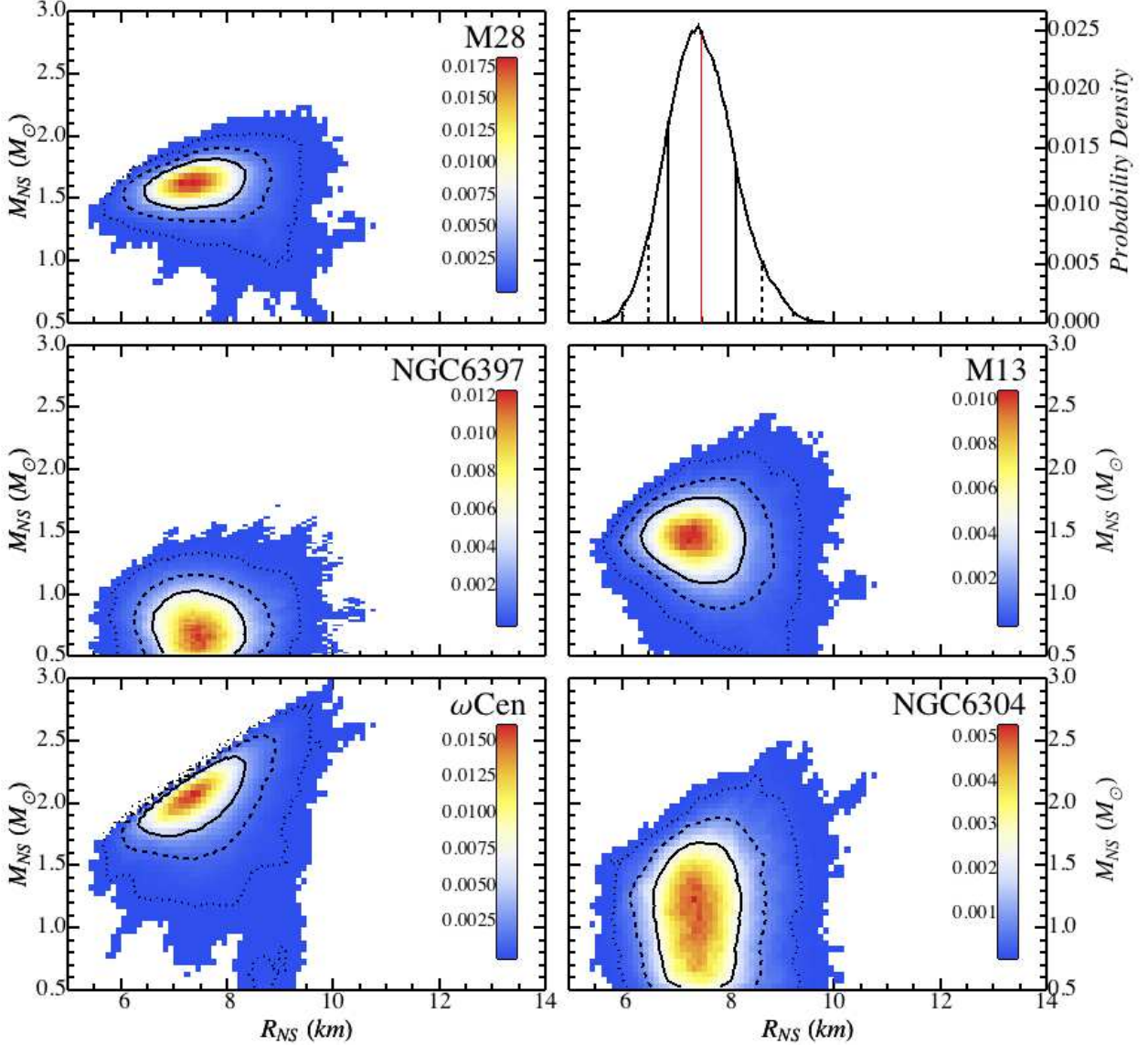


FIG. 13.— Figure similar to Figure 9, showing results of Run #5. The hydrogen column density N_H is left free in this run, but the distances remained fixed, and no PL component was added. This run produced $R_{NS} = 7.5^{+1.1}_{-1.0}$ km.

Finally, the approach of this paper is not dissimilar to the work of Steiner et al. (2010, 2012) in the sense that different targets are combined to produce constraints on the dEoS. However, our analysis imposes R_{NS} to be quasi-constant for all the targets, as justified by recent observations favoring “normal matter” dEoSs. Other differences include two qLMXBs (M28 and NGC 6304) added to the present analysis, and the qLMXB in 47 Tuc not used here because of the uncertainties related to pile-up. Finally, the work of Steiner et al. (2010, 2012) uses type-I X-ray burst sources, which are not considered in the present analysis.

5.2. Possible biases resulting from the analysis

5.2.1. Non-zero power-law for NGC 6397

The runs that included a PL component (#3, #4, and #7, with photon index $\Gamma = 1$) resulted in PL normalizations consistent with zero for all targets, except for NGC 6397. Specifically, $\text{Norm}_{\text{PL,NGC 6397}} = 2.7^{+1.3}_{-1.3} \times 10^{-7} \text{ keV}^{-1} \text{ s}^{-1} \text{ cm}^{-2}$, which is not consistent with zero, at the 3.4σ level, in Run #7. This indicates a possible non-negligible contribution of a PL above ~ 2 keV. Using *XSPEC* (without the MCMC approach), the spectra of NGC 6397 are fitted without the other qLMXBs, and the PL normalization obtained is $\text{Norm}_{\text{PL}} = 2.1^{+1.3}_{-1.3} \times 10^{-7} \text{ keV}^{-1} \text{ s}^{-1} \text{ cm}^{-2}$ which corresponds to a contribution of $2.6^{+1.7}_{-1.7}\%$ of the total unabsorbed flux of NGC 6397 in the 0.5–10 keV energy band. Such a contribution is consistent with that measured in

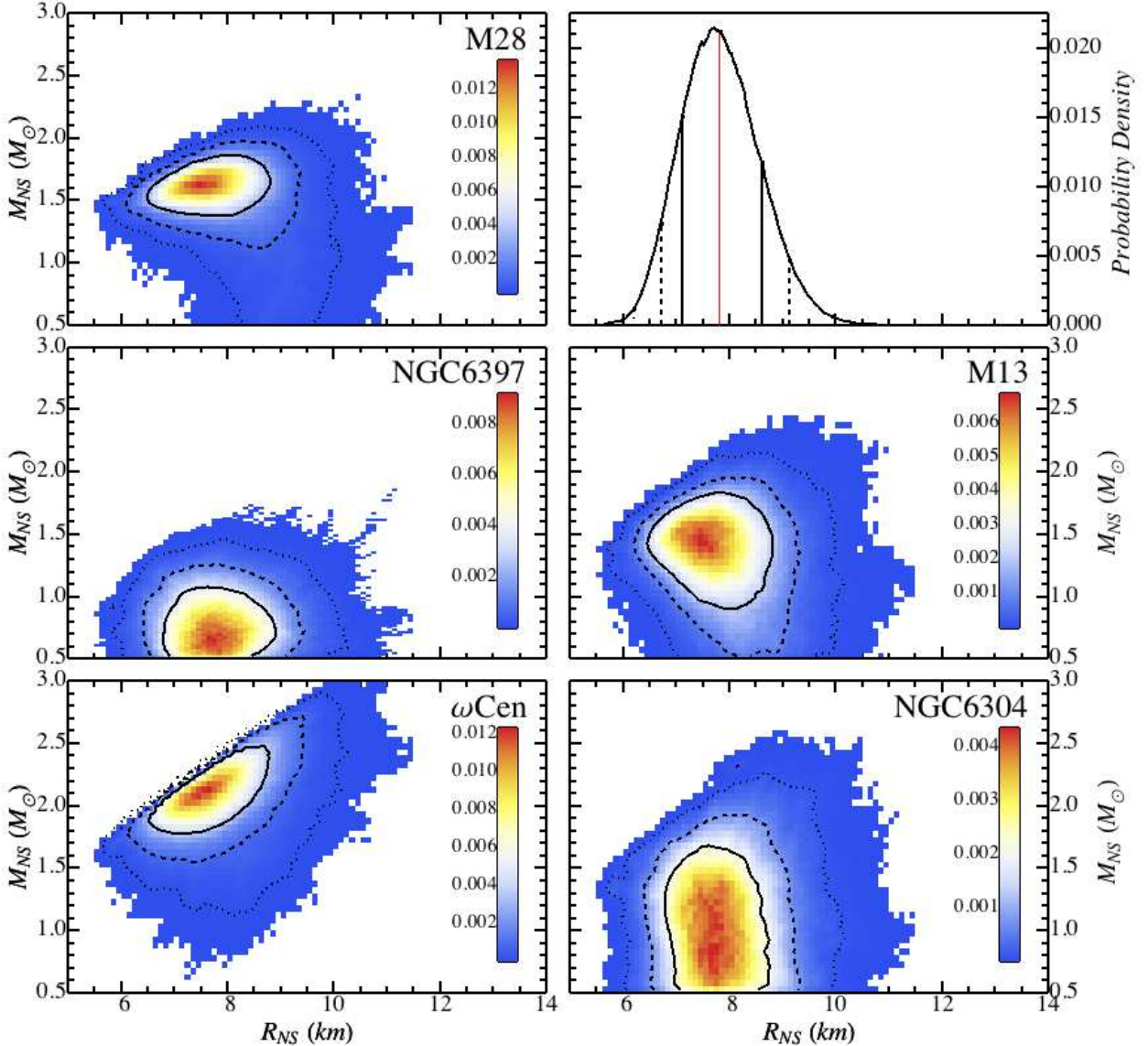


FIG. 14.— Figure similar to Figure 9, but for the MCMC Run #6. The characteristics of this run include N_H values free to vary in the fit, and the presence of the Gaussian Bayesian priors for the distances. No PL component was included in run. A value $R_{NS} = 7.8^{+1.3}_{-1.1}$ km was found.

the previous results, $\leq 3.3\%$ (Guillot et al. 2011a), for the same photon index.

Nonetheless, adding a PL contribution for each target does not significantly bias the posterior distribution of R_{NS} . Specifically, adding PL components between Runs #1 and #3 changed the radius measurement from $R_{NS} = 7.1^{+0.5}_{-0.6}$ km (Run #1) to $R_{NS} = 7.3^{+0.5}_{-0.6}$ km (Run #3); between Runs #2 and #4, R_{NS} changed from $R_{NS} = 7.6^{+0.9}_{-0.9}$ km (Run #2) to $R_{NS} = 8.0^{+1.0}_{-1.0}$ km (Run #4). Between runs #6 and #7 (free N_H), the R_{NS} distributions changed more significantly, but they are nonetheless consistent: $R_{NS} = 7.8^{+1.3}_{-1.1}$ km (Run #6) to $R_{NS} = 9.1^{+1.3}_{-1.5}$ km (Run #7). Therefore, adding PL com-

ponents does not significantly change the R_{NS} posterior distribution, but nonetheless includes systematic uncertainties related to the possible presence of a PL component into the measured R_{NS} . With the limited PL contributions observed ($< 5\%$), the choice of photon index does not affect the `nsatmos` component. This is tested on NGC 6397 alone, the qLMXB with the strongest PL contribution, where the PL photon index is changed from $\Gamma = 1$ to $\Gamma = 2$. Such a change results in consistent PL contributions, but more importantly, it results in a non-significant increase of only $\sim 1\%$ in the value of R_{NS} , well within the uncertainties of the measurement. Other parameters such as the mass, temperature and the PL normalization are consistent between the two trials, with

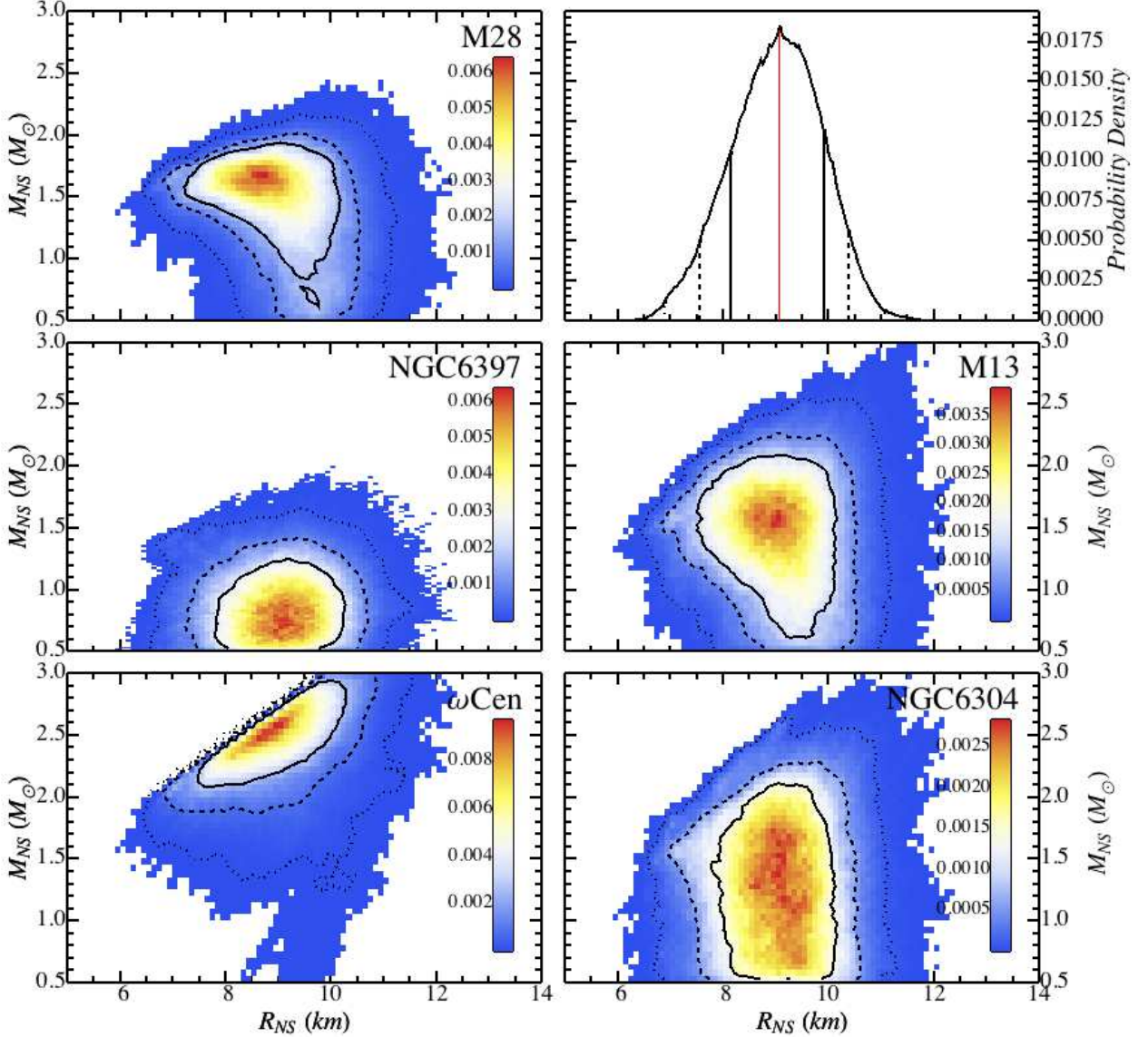


FIG. 15.— Figure similar to Figure 9, corresponding to Run #7. Here, all the possible assumptions have been relaxed to obtain a R_{NS} measurement the least affected by systematic uncertainties. The N_H parameters are left free; and Gaussian Bayesian priors and PL components are included. This results in an R_{NS} measurement: $R_{\text{NS}} = 9.1^{+1.3}_{-1.3}$ km

$\Gamma = 1$ and with $\Gamma = 2$. Given that NGC 6397 has the strongest PL contribution and that changing the photon index from $\Gamma = 1$ to $\Gamma = 2$ does not modify R_{NS} , it is expected to be the same for the simultaneous spectral analysis.

5.2.2. Effects of Individual Targets on the Simultaneous Fit

An additional set of MCMC runs was performed to investigate whether some targets have a dominant biasing effect on the simultaneous spectral fitting presented above. This analysis is performed by excluding each target individually and observing the resulting marginalized posterior distributions of the parameters. Results are listed in Table 8. These runs were performed like Run

#7, i.e., with the N_H value free, with Gaussian Bayesian priors on the distances, and with the additional PL component. The values of R_{NS} obtained when removing each target are all consistent within 2σ of each other, and more importantly, consistent with the R_{NS} distribution obtained when all targets are included (Run #7, in Table 6). Similarly, the kT_{eff} , M_{NS} , R_{∞} and the α_{pileup} values of each targets are consistent with each other in all five cases presented in Table 8, and also consistent with the values from Run #7. Overall, no individual target has any dominant effect on the simultaneous fit. This ensures that no qLMXB induces a significant bias on R_{NS} . This is also compatible with recent results (Steiner et al. 2012), obtained by combining $M_{\text{NS}}-R_{\text{NS}}$ distributions of

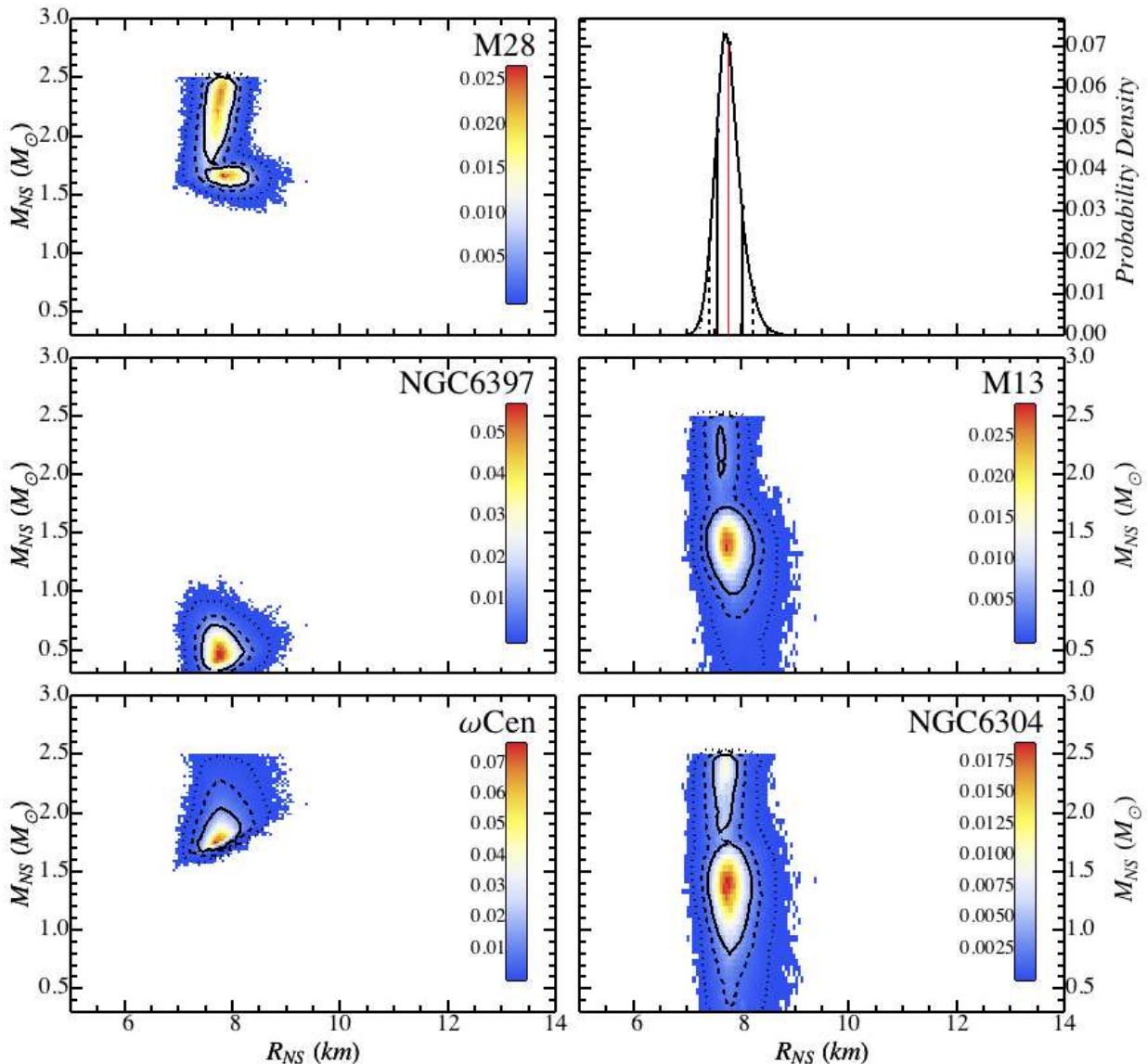


FIG. 16.— Figure similar to Figure 9, i.e., Run #1 with fixed distances instead of Gaussian Bayesian priors, fixed N_H values, and no PL component included. The only difference resides in the H-atmosphere model, where `nsaggrav` model was used instead of `nsatmos`. Note that the parameter limits in `nsaggrav` are [6–20] km for R_{NS} , and [0.4–2.5] M_\odot for M_{NS} . The R_{NS} measurement, $R_{NS} = 7.8^{+0.5}_{-0.3}$ km, is consistent with that of Run #1, but the some of the M_{NS} – R_{NS} posterior distributions are significantly different from those of Figure 9. This is further discussed in Section 4.2.

qLMXBs and type-I X-ray bursts. In that work, it was demonstrated that removing extreme cases (for example the qLMXB X7 in 47Tuc, or the qLMXB in M13) had no or little effect on the resulting empirical dEoS.

For completeness, and to confirm this observation, a spectral analysis combining X7 to the other five qLMXBs of this work is performed in *XSPEC* in order to determine R_{NS} . Note that the MCMC approach is not used and is not necessary here since this additional analysis is simply a consistency check to determine if outliers can have an impact of the best-fit R_{NS} measurement¹⁴.

Furthermore, Gaussian Bayesian priors are not used for this consistency check. The spectral data available for X7 and used here are described in a previous work (Heinke et al. 2006). For the distance to the qLMXB, we used the weighted average of all recent distance estimates listed in another reference (Woodley et al. 2012), i.e., $d_{47Tuc} = 4.52$ kpc. The resulting best-fit NS radius found was $R_{NS} = 7.0^{+1.0}_{-2.0p}$ km with the acceptable statis-

of the present work because of the unquantified systematic errors associated with the correction of the large amount of pile-up affecting the spectra, and its uncertain effect on our final statistical error bars.

¹⁴ As mentioned before, X7 was not used in the main analysis

tics χ^2/dof (prob.) = 0.98/1003 (0.70). This result is consistent with the R_{NS} measurement of Run #1 (performed without adding the spectra of X7) and seem to confirm that outliers, such as the qLMXB X7 in 47Tuc, do not affect the radius measurement, as demonstrated in a previous work (Steiner et al. 2012).

5.2.3. Composition of the Neutron Star Atmosphere

The $M_{\text{NS}}-R_{\text{NS}}$ measurements of NSs in qLMXBs rely on the atmosphere modeling, which itself relies on a major assumption of this work, namely the composition of the NS atmosphere. It is generally assumed that NS atmosphere are composed exclusively of pure hydrogen (e.g., Rutledge et al. 2002; Heinke et al. 2006), since heavier accreted elements will settle through the atmosphere on short time scales (Bildsten et al. 1992). NS He atmospheres could be observed in the case of He accretion from WD donors in ultra-compact X-ray binaries. An He-atmosphere model was used to fit the spectra of M28 and led to a radius $1.5\times$ larger than that obtained with a H-atmosphere, favoring stiff dEoSs (Servillat et al. 2012). Similarly, for the qLMXB in M13, assuming a He composition of the NS atmosphere increases the radius R_{NS} by a factor ~ 1.2 (Catuneanu et al. 2013).

The actual composition of the NS atmosphere can be inferred from the identification of the donor companion star, which proves a difficult task in the crowded environment of GCs. Only two GC qLMXBs have identified counterparts, X5 in 47Tuc (Edmonds et al. 2002), and in ω Cen (Haggard et al. 2004), both of which discovered from their strong H α emission, indicating hydrogen donor stars.

5.2.4. Causality Limit

With the assumptions made and the model chosen in the present work, parts of the $M_{\text{NS}}-R_{\text{NS}}$ contours resulting from the analysis cover a section of the parameter space that goes past the causality limit as set in earlier works (Lattimer et al. 1990; Lattimer & Prakash 2001). Stricter constraints on the $M_{\text{NS}}-R_{\text{NS}}$ contours could be obtained by imposing that the sets of MCMC accepted points ($R_{\text{NS}}, M_{\text{NS}}$) all obey $R_{\text{NS}} \geq 3GM_{\text{NS}}/c^2$, i.e., do not cross the causality line. However, we choose not to change constraints; this produces a larger error region than may be necessary (if one were to explicitly adopt causality as an assumption), but the goal of this analysis is to produce the most conservative, assumption-free uncertainty region for R_{NS} . Only if much higher S/N data were obtained, and the M-R parameter space required (or strongly preferred) a value in the region excluded by the causality requirement cited above (Lattimer et al. 1990) would it become necessary to revisit this assumption.

5.2.5. Effect of Assumptions

As discussed in this paper, assumptions can have a strong effect on the interpretation of spectral fits of individual sources and consequently on the simultaneous spectral analysis as well. The selection of the distances to the GCs (fixed or with Gaussian Bayesian priors) can skew the R_{NS} measurement toward smaller or larger values. For instance, in early runs of this analysis, the distance $d_{\text{M28}} = 5.1 \pm 0.5$ kpc (Rees & Cudworth 1991) was initially used, before it was updated to a more

TABLE 8
EFFECT OF INDIVIDUAL TARGETS ON THE SIMULTANEOUS SPECTRAL FIT

Target excluded	R_{NS} (km)	$\chi^2/\text{d.o.f.}$ (prob.)	Accept. rate
NONE (Run #7)	$9.1^{+1.3}_{-1.5}$ km	0.98 / 628 (0.64)	7%
WITHOUT M28	$8.4^{+1.5}_{-1.3}$ km	0.98 / 381 (0.69)	7%
WITHOUT NGC 6397	$10.7^{+1.7}_{-1.4}$ km	0.89 / 428 (0.95)	9%
WITHOUT M13	$8.6^{+1.5}_{-1.3}$ km	0.94 / 588 (0.86)	7%
WITHOUT ω Cen	$8.7^{+1.5}_{-1.4}$ km	0.95 / 601 (0.81)	8%
WITHOUT NGC 6304	$9.0^{+1.5}_{-1.4}$ km	0.93 / 622 (0.88)	8%

NOTE. — The spectral fits in this table were performed following Run #7, with free N_H values, Gaussian Bayesian priors on the distances and with an additional PL components in the model. Each target were successively removed to investigate the possible effect of individual sources on the global fit. The R_{NS} values obtained in each of these five tests are consistent with each other, and with that of Run #7. This confirms that none of the five qLMXBs significantly skews the R_{NS} measurement. Quoted uncertainties are 90% confidence, and values in parentheses are held fixed.

recent value $d_{\text{M28}} = 5.5 \pm 0.3$ kpc (Testa et al. 2001; Servillat et al. 2012). This caused the R_{NS} measurement (of Run #7) to change from $R_{\text{NS}} = 8.7^{+1.3}_{-1.1}$ km to $R_{\text{NS}} = 9.1^{+1.3}_{-1.5}$ km as the distance of M28 was increased. The values are consistent with each other, but this larger d_{M28} shifted the R_{NS} measurement. This is expected since the normalization of a thermal spectrum is $\propto (R_{\infty}/d)^2$.

Another strongly influential parameter is the galactic absorption. A change in N_H will strongly affect the M_{NS} and R_{NS} best-fit. Specifically, a decrease (increase) in N_H results in an decrease (increase) in R_{∞} , respectively. This was shown for NGC 6397 and ω Cen, in Section 4.1. For NGC 6397, the HI-survey N_H value ($N_{H,22} = 0.14$) leads to a $R_{\infty} = 11.8^{+0.8}_{-0.7}$ km, while the X-ray deduced value ($N_{H,22} = 0.096^{+0.017}_{-0.015}$) produces $R_{\infty} = 8.4^{+1.3}_{-1.1}$ km, a decrease of $\sim 30\%$. For ω Cen, the best-fit R_{∞} almost doubles as the constraint on N_H is relaxed, causing the value to increase from $N_{H,22} = 0.09$ (HI-survey) to $N_{H,22} = 0.182^{+0.041}_{-0.047}$. Consequently, using assumptions for the N_H values, like those derived from HI-surveys, can lead to strongly skewed R_{NS} measurements.

Consequently, it is preferable to avoid using assumed values, when possible, and therefore the R_{NS} measurement from Run #7 is presented as the final result of this work.

5.3. The R_{NS} measurement

The goal of this paper being to measure R_{NS} , the following discussion is focused on the R_{NS} posterior distributions, on the comparison with other R_{NS} measurement, and on the implication that such a radius measurement will have for the determination of the dEoS.

The striking observation one can make pertains to the low range of values of the resulting R_{NS} distributions obtained from the different runs. The R_{NS} distributions remained below $R_{\text{NS}} < 10.4$ km (90%-confidence), or $R_{\text{NS}} < 11.1$ km (99%-confidence). This resulted from Run #7 (see Figure 15), where a particular effort was made to consider all possible sources of systematic uncertainties. The result from Run #7 is the most general R_{NS}

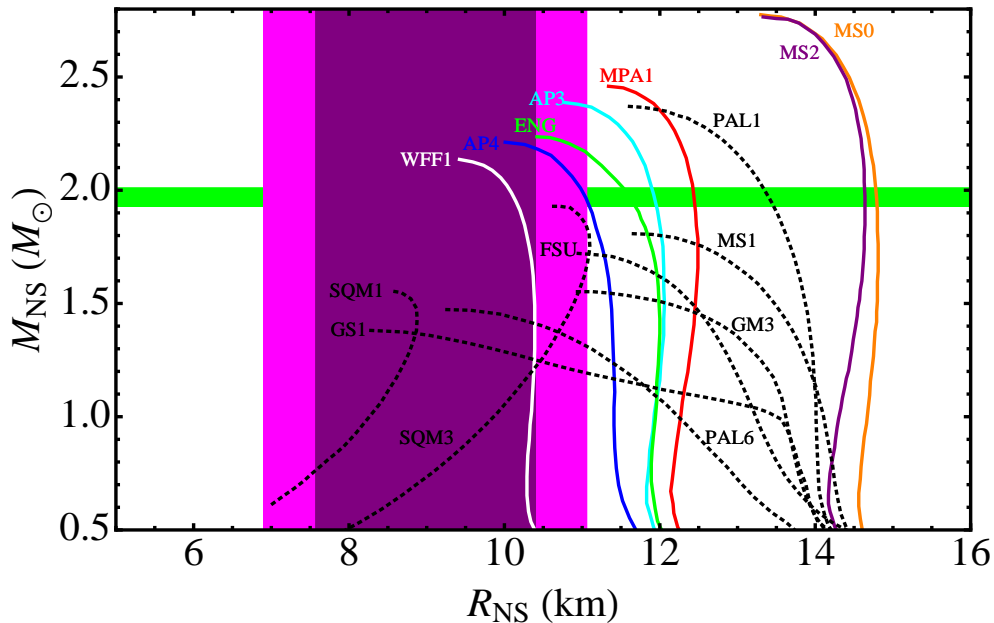


FIG. 17.— Figure showing the constraint on the dEoS imposed by the radius measurement obtained in this work: $R_{\text{NS}} = 9.1^{+1.3}_{-1.5}$ km (90%-confidence). The dark and light shaded areas show the 90%-confidence and 99%-confidence constraints of the R_{NS} measurement, respectively. The mass measurement of PSR J1614-2230 is shown as the horizontal band (Demorest et al. 2010). “Normal matter” EoSs are the colored solid lines. Other types of EoSs, such as the hybrid or quark-matter EoSs are included for comparison, with dashed lines. As mentioned in Section 5, the present analysis only places constraints on the “normal matter” EoSs since they are the only family of EoSs included in our assumptions. Among them, only the very soft dEoSs (such as WFF1, Wiringa et al. 1988) are consistent with the radius obtained here. The EoS are obtained from Lattimer & Prakash (2001, 2007).

distribution, i.e., with the fewest assumptions, that can be produced. Also, the progressive relaxation of the assumptions throughout the analysis demonstrated that no unexpected behavior was present in the final $M_{\text{NS}}-R_{\text{NS}}$ distributions of Run #7 and that the resulting low-value of R_{NS} was not affected by systematics.

Previous works reported low values of NS radii, but these measurements have high uncertainties due to low S/N, leading to poorly constrained R_{NS} and M_{NS} (e.g., in NGC 2808, Webb & Barret 2007; Servillat et al. 2008). Another qLMXB in NGC 6553 was identified with a small radius, $R_{\text{NS}} = 6.3^{+2.3}_{-0.8}$ km (90%-confidence) for $M_{\text{NS}} = 1.4 M_{\odot}$ (Guillot et al. 2011b). However, low-S/N *Chandra* observations demonstrated that the *XMM* spectra of the source was affected by hard X-ray contamination from a marginally resolved nearby source. Higher-S/N observations with *Chandra* are necessary to confirm the qLMXB classification and produce the uncontaminated spectrum necessary for its use in the present analysis.

In addition to qLMXB R_{NS} measurements, low radii were found from the analysis of photospheric radius expansion type-I X-ray bursts. A review of the method used to determine R_{NS} from these sources can be found in the literature (Özel 2006; Suleimanov et al. 2011b). The LMXBs EXO 1745-248, 4U 1608-52, and 4U 1820-30 were found to have respective radii in the 2σ ranges $R_{\text{NS}} = [7.5 - 11.0]$ km (Özel et al. 2009), $R_{\text{NS}} = [7.5 - 11.5]$ km (Güver et al. 2010a) and $R_{\text{NS}} = [8.5 - 9.5]$ km (Güver et al. 2010b), respectively. While these results are on a par with what is found in this paper, controversy emerged with the realization that the analysis presented in the cited works was not internally consistent because the most probable observables (from Monte-Carlo sam-

pling) led to imaginary masses and radii (Steiner et al. 2010). Relaxing the assumption that the photospheric radius equals the physical radius R_{NS} at touchdown led to real-valued solutions of M_{NS} and R_{NS} , and to larger upper limits for the radius. Furthermore, it is argued in a later work that the short bursts from EXO 1745-248, 4U 1608-52 and 4U 1820-30 are not appropriate for such analysis because the post-burst cooling evolution of these sources does not match the theory of passively cooling NSs (Suleimanov et al. 2011a). Therefore, the $M_{\text{NS}}-R_{\text{NS}}$ constraints from type I X-ray bursts should be considered with these results in mind.

More recently, distance independent constraints in $M_{\text{NS}}-R_{\text{NS}}$ space were produced from the analysis of the sub-Eddington X-ray bursts from the type I X-ray burster GS 1826-24 (Zamfir et al. 2012). That analysis, performed for a range of surface gravities ($\log_{10}(g) = 14.0, 14.3, 14.6$) and a range of H/He abundances ($0.01 Z_{\odot}, 0.1 Z_{\odot}$ and Z_{\odot}) led to radii $R_{\text{NS}} \lesssim 11.5$ km. While distance-independent, the results are highly influenced by the atmosphere composition and metallicity. For pure He composition, the upper limit of R_{NS} becomes $R_{\text{NS}} \lesssim 15.5$ km (Zamfir et al. 2012).

Finally, the multiwavelength spectral energy distribution of the isolated neutron star RX J185635-3754 was analyzed to produce small values of R_{NS} and M_{NS} with no plausible dEoS consistent with these values: $R_{\text{NS}} \sim 6$ km and $M_{\text{NS}} \sim 0.9 M_{\odot}$ for $d = 61$ pc (Pons et al. 2002). A recent distance estimation to the source $d = 123^{+11}_{-15}$ pc (Walter et al. 2010) led to revised values: $R_{\text{NS}} = 11.5 \pm 1.2$ km and $M_{\text{NS}} = 1.7 \pm 1.3 M_{\odot}$ (Steiner et al. 2012). While this result is consistent with the R_{NS} measurement obtained in this paper and with the other works reporting low- R_{NS} values, it has to

be taken with care since the high-magnetic field of the source is not accounted for in the spectral model used by the original analysis.

Recently, it was shown that the dEoS can be empirically determined from $M_{\text{NS}}-R_{\text{NS}}$ measurements of NS, using the thermal spectra of qLMXBs and the photospheric radius expansion of X-ray bursts (Steiner et al. 2010). This method uses MCMC simulation and Bayesian priors to determine the most probable dEoS parameters, and equivalently, the corresponding most probable $M_{\text{NS}}(R_{\text{NS}})$ for NS. In a recent paper, this method was used with four X-ray bursting sources and four GC qLMXBs. Considering all scenarios, the 2σ lower and upper limits for R_{NS} are 9.17 km and 13.92 km (Steiner et al. 2012). The R_{NS} distribution of the present paper $R_{\text{NS}} = 9.1_{-1.5}^{+1.3}$ km (90%-confidence, from Run #7) is consistent with several of the model variations of Steiner et al. (2012), namely variation C (dEoS parameterized with uniform prior in the pressure at four energy density values), variation CII (same as previous, but with low value of the color correction, $1 < f_C < 1.35$), variation AII/AIII (dEoS parameterized as two piecewise continuous power-laws, with $1 < f_C < 1.35$), see Steiner et al. (2012) for details about the variations of the model. Variation E (dEoS for quark stars) is incompatible with our original assumption that R_{NS} is quasi-constant for a large range of M_{NS} above $0.5 M_{\odot}$.

Theoretical EoSs have been proposed for more than two decades. A non-exhaustive list can be found in the literature (Lattimer & Prakash 2001, 2007). When comparing the resulting R_{NS} distribution to proposed theoretical “normal matter” dEoSs, one can note that most of those are not consistent with the low- R_{NS} result presented in this work. Indeed, most of the dEoSs describing “normal matter” correspond to radii larger than 11.5 km (see Figure 17). A spread in R_{NS} is observed in these dEoSs at large masses, in the part of the $M_{\text{NS}}-R_{\text{NS}}$ diagram where the compact object approaches collapse. However, this breadth of the R_{NS} variation for a given dEoS is well within the uncertainties obtained in this work. Overall, the radius measurement $R_{\text{NS}} = 9.1_{-1.5}^{+1.3}$ km constrains the dEoS to those consistent with low- R_{NS} , such as WFF1 (Wiringa et al. 1988). Note that this analysis cannot address the veracity of more exotic types of EoSs (hybrid and SQM) or any dEoS which does not predict a quasi-constant R_{NS} within the observable mass range.

It is known that R_{NS} is related to fundamental nuclear physics parameters, such as the symmetry energy (Horowitz & Piekarewicz 2001b,a). We expect the present constraints on R_{NS} can be used to constrain this, and other properties of dense nuclear matter. We leave this for future work.

It has been pointed out (Lattimer & Prakash 2010) that an argument regarding a maximally compact neutron star (Koranda et al. 1997) results in a relationship between the maximal neutron star radius (R_{max}) and the maximal neutron star mass (M_{max}) for a given equation of state:

$$\frac{R_{\text{max}}}{M_{\text{max}}} = 2.824 \frac{G}{c^2} \quad (4)$$

where G is Newton’s constant and c is the speed of light. Adopting this, the 99% confidence upper limit is $M_{\text{max}} < 2.66 M_{\odot}$, which does not violate any measured neutron

star masses at present.

The small- R_{NS} value found in this paper, and other low- R_{NS} results cited above, are consistent with soft dEoSs such as WFF1. However, results of M_{NS} and R_{NS} measurements from other sources seem to favor stiffer dEoSs. The qLMXB 47Tuc X7 has a reported radius $R_{\text{NS}} = 14.5_{-1.4}^{+1.6}$ km for $M_{\text{NS}} = 1.4 M_{\odot}$ (Heinke et al. 2006), supporting stiff dEoSs, such as MS0/2 (Müller & Serot 1996). Nonetheless, the range of radii allowed by the published $M_{\text{NS}}-R_{\text{NS}}$ contours for X7 is consistent with the radius measurement presented in the present work. Moreover, the X7 $M_{\text{NS}}-R_{\text{NS}}$ contours are compatible with the dEoS WFF1 (Wiringa et al. 1988). Another work used the long photospheric radius expansion X-ray bursts from 4U 1724-307 to conclude that stiff dEoSs are describing the dense matter inside NSs (Suleimanov et al. 2011a). Specifically, it was found that $R_{\text{NS}} > 13.5$ km for $M_{\text{NS}} < 2.3 M_{\odot}$, and for a range for NS atmospheric composition. Lower R_{NS} values, in the range 10.5–17 km, are allowed for $M_{\text{NS}} > 2.3 M_{\odot}$, for pure H or solar metallicity composition. This radius measurement is only marginally consistent with the present work for large masses, $M_{\text{NS}} > 2.3 M_{\odot}$, which implies a dEoS capable of reaching $M_{\text{NS}} \sim 2.3 M_{\odot}$ for $R_{\text{NS}} \sim 10 - 11$ km. Finally, another radius measurement, obtained by modeling the thermal pulses of the millisecond pulsar PSR J0437–4715 (Bogdanov 2012), led to values, $R_{\text{NS}} > 11$ km (3σ), is inconsistent with the measurement presented in our work.

6. SUMMARY

In this paper, we measured R_{NS} using the assumption that the radius is quasi-constant for a wide range of M_{NS} larger than $M_{\text{NS}} > 0.5 M_{\odot}$, i.e., constant within the measurement precision. This is justified by recent observations favoring “normal matter” dEoSs which are described by this characteristic. For this analysis, the spectra from five GCs qLMXBs observed with the *Chandra X-ray Observatory* and *XMM-Newton* were used in a simultaneous analysis, constraining R_{NS} to be the same for all targets.

For this, we used an MCMC approach to spectral fitting, which offers several advantages over the Levenberg-Marquardt χ^2 -minimization technique generally used for spectral fits. For example, the MCMC framework allows imposing Bayesian priors to parameters, namely the distance to the host GCs. By doing so, the distance uncertainties are included into the posterior R_{NS} distribution. In addition, one can marginalize the posterior distributions over any parameters and very easily obtain $M_{\text{NS}}-R_{\text{NS}}$ distributions, while the grid-search method in *XSPEC* can be problematic in the case of spectral fits with many free parameters and complicated χ^2 -space. The algorithm chosen in this work is an affine-invariant ensemble sampler, commonly called “Stretch-Move” algorithm, which is particularly appropriate (i.e., converging efficiently) for elongated and curved distributions.

The principal result of the simulations performed in this analysis is that NSs are characterized by small physical radii. Specifically, when the distances and Galactic absorption parameters are fixed, $R_{\text{NS}} = 7.1_{-0.6}^{+0.5}$ km (from Run #1). A more general posterior distribution for R_{NS} i.e., less prone to systematic biases, is obtained

by applying Gaussian Bayesian priors for the five GC distance, by freeing the N_H parameters, and by adding a PL component to the model to account for a possible spectral component at high photon energies. Such a spectral component could be the largest possible source of uncertainty, and could be skewing R_{NS} downward, but it is accounted for in the last and most relaxed MCMC run. In fact, such a spectral component was discovered herein for NGC 6397.

The progressive relaxation of assumptions led us to a good understanding of the spectral fit in Run #7, minimizing systematic uncertainties. Therefore, with the H-atmosphere model `nsatmos`, the measured NS radius is $R_{NS} = 9.1^{+1.3}_{-1.5}$ km (from Run #7). These results are compatible with other low- R_{NS} measurements from GC qLMXBs or type-I X-ray bursts, but not consistent with some published R_{NS} measurement leading to values $R_{NS} > 11$ km. We recommend these R_{NS} constraints, from Run #7, be those relied upon for constraints on the dEoS and other nuclear physics model parameters, as this run has the fewest associated assumptions behind it.

Among the dEoS listed in previous works (Lattimer & Prakash 2001, 2007), the R_{NS} mea-

surement presented here is only compatible with “normal matter” dEoSs consistent with $R_{NS} \sim 10$ km, e.g. WFF1 (Wiringa et al. 1988). Most dEoSs are compatible with larger radii, at $R_{NS} \gtrsim 12$ km and above. Given the results presented in this work, the theory of dense nuclear matter may need to be revisited.

The authors would like to thank the referee for useful remarks that improved the clarity of this article. SG is a Vanier Canada Graduate Scholar and acknowledges the support of NSERC via the Vanier CGS program. RER is supported by an NSERC Discovery grant. MS acknowledges supports from NASA/Chandra grant GO0-11063X and the Centre National d’Études Spatiales (CNES). The authors would like to thank Keith A. Arnaud and Craig Gordon for their precious help with the use of *XSPEC* and *PyXSPEC*. The authors are also very grateful toward René Breton for sharing his python implementation of the “Stretch-Move” algorithm. Finally, the authors also acknowledge the use of archived *XMM* and *Chandra* data from the High Energy Astrophysics Archive Research Center Online Service, provided by the NASA GSFC.

REFERENCES

- Akmal, A. & Pandharipande, V. R. 1997, *Phys. Rev. C*, 56, 2261
 Baumgardt, H. 2008, *Astronomische Nachrichten*, 329, 881
 Baumgardt, H. & Kroupa, P. 2005, in *ESA Special Publication*, Vol. 576, *The Three-Dimensional Universe with Gaia*, ed. C. Turon, K. S. O’Flaherty, & M. A. C. Perryman, 681
 Becker, W. et al. 2003, *ApJ*, 594, 798
 Bednarek, I., Haensel, P., Zdunik, J. L., Bejger, M., & Mańka, R. 2011, *ArXiv e-prints*
 Bica, E., Bonatto, C., Barbuy, B., & Ortolani, S. 2006, *A&A*, 450, 105
 Bildsten, L., Salpeter, E. E., & Wasserman, I. 1992, *ApJ*, 384, 143
 Bogdanov, S. 2012, *ArXiv e-prints*
 Bogdanov, S., Grindlay, J. E., & Rybicki, G. B. 2008, *ApJ*, 689, 407
 Bono, G., Caputo, F., & Di Criscienzo, M. 2007, *A&A*, 476, 779
 Bovy, J., Rix, H.-W., Liu, C., Hogg, D. W., Beers, T. C., & Lee, Y. S. 2012, *ApJ*, 753, 148
 Brown, E. F. 2000, *ApJ*, 531, 988
 Brown, E. F., Bildsten, L., & Rutledge, R. E. 1998, *ApJ*, 504, L95+
 Cackett, E. M., Brown, E. F., Miller, J. M., & Wijnands, R. 2010, *ApJ*, 720, 1325
 Campana, S., Stella, L., Mereghetti, S., & Cremonesi, D. 2000, *A&A*, 358, 583
 Caprio, M. A. 2005, *Computer Physics Communications*, 171, 107
 Catuneanu, A., Heinke, C. O., Sivakoff, G. R., Ho, W. C. G., & Servillat, M. 2013, *ArXiv e-prints*
 Davidge, T. J., Cote, P., & Harris, W. E. 1996, *ApJ*, 468, 641
 Davis, J. E. 2001, *ApJ*, 562, 575
 Demorest, P. B., Pennucci, T., Ransom, S. M., Roberts, M. S. E., & Hessels, J. W. T. 2010, *Nature*, 467, 1081
 Dickey, J. M. & Lockman, F. J. 1990, *ARA&A*, 28, 215
 Edgar, R. J. & Vikhlinin, A. A. 2004, *Chandra X-ray Center Calibration Memo*, available at http://cxc.harvard.edu/cal/Acis/Cal_prods/qe/qe_memo.ps
 Edmonds, P. D., Heinke, C. O., Grindlay, J. E., & Gilliland, R. L. 2002, *ApJ*, 564, L17
 Engvik, L., Osnes, E., Hjorth-Jensen, M., Bao, G., & Ostgaard, E. 1996, *ApJ*, 469, 794
 Foreman-Mackey, D., Hogg, D. W., Lang, D., & Goodman, J. 2012, *ArXiv e-prints*
 Gendre, B., Barret, D., & Webb, N. A. 2003a, *A&A*, 400, 521
 — 2003b, *A&A*, 403, L11
 Glendenning, N. K. & Moszkowski, S. A. 1991, *Physical Review Letters*, 67, 2414
 Glendenning, N. K. & Schaffner-Bielich, J. 1999, *Phys. Rev. C*, 60, 025803
 Goodman, J. & Weare, J. 2010, *CAMCoS*, 5, 65
 Graessle, D. E., Evans, I. N., Glotfelty, K., He, X. H., Evans, J. D., Rots, A. H., Fabbiano, G., & Brissenden, R. J. 2007, *Chandra News*, 14, 33
 Gratton, R. G., Carretta, E., Bragaglia, A., Lucatello, S., & D’Orazi, V. 2010, *A&A*, 517, A81
 Grebel, E. K. & Roberts, W. J. 1995, *A&AS*, 109, 293
 Gregory, P. 2005, *Bayesian Logical Data Analysis for the Physical Sciences* (New York, NY, USA: Cambridge University Press)
 Grindlay, J. E., Heinke, C. O., Edmonds, P. D., Murray, S. S., & Cool, A. M. 2001, *ApJ*, 563, L53
 Guainizzi, M. 2012, *XMM-Newton Calibration Technical Note*, available at <http://xmm2.esac.esa.int/docs/documents/CAL-TN-0018.pdf>
 Guillot, S., Rutledge, R. E., Bildsten, L., Brown, E. F., Pavlov, G. G., & Zavlin, V. E. 2009a, *MNRAS*, 392, 665
 Guillot, S., Rutledge, R. E., & Brown, E. F. 2011a, *ApJ*, 732, 88
 Guillot, S., Rutledge, R. E., Brown, E. F., Pavlov, G. G., & Zavlin, V. E. 2009b, *ApJ*, 699, 1418
 — 2011b, *ApJ*, 738, 129
 Gupta, S., Brown, E. F., Schatz, H., Möller, P., & Kratz, K.-L. 2007, *ApJ*, 662, 1188
 Güver, T., Özel, F., Cabrera-Lavers, A., & Wroblewski, P. 2010a, *ApJ*, 712, 964
 Güver, T., Wroblewski, P., Camarota, L., & Özel, F. 2010b, *ApJ*, 719, 1807
 Haakonsen, C. B., Turner, M. L., Tacik, N. A., & Rutledge, R. E. 2012, *ApJ*, 749, 52
 Haensel, P. & Zdunik, J. L. 1990, *A&A*, 227, 431
 — 2008, *A&A*, 480, 459
 Haggard, D., Cool, A. M., Anderson, J., Edmonds, P. D., Callanan, P. J., Heinke, C. O., Grindlay, J. E., & Bailyn, C. D. 2004, *ApJ*, 613, 512
 Hansen, B. M. S. et al. 2007, *ApJ*, 671, 380
 Harris, W. E. 1996, *AJ*, 112, 1487
 — 2010, *ArXiv e-prints*
 Heinke, C. O., Grindlay, J. E., Lloyd, D. A., & Edmonds, P. D. 2003, *ApJ*, 588, 452
 Heinke, C. O., Rybicki, G. B., Narayan, R., & Grindlay, J. E. 2006, *ApJ*, 644, 1090
 Heyl, J. S. et al. 2012, *ArXiv e-prints*
 Ho, W. C. G. & Heinke, C. O. 2009, *Nature*, 462, 71
 Horowitz, C. J. & Piekarewicz, J. 2001a, *Phys. Rev. C*, 64, 062802

- 2001b, *Physical Review Letters*, 86, 5647
- Kalberla, P. M. W., Burton, W. B., Hartmann, D., Arnal, E. M., Bajaja, E., Morras, R., & Pöppel, W. G. L. 2005, *A&A*, 440, 775
- Koranda, S., Stergioulas, N., & Friedman, J. L. 1997, *ApJ*, 488, 799
- Lai, X.-Y. & Xu, R.-X. 2011, *Research in Astronomy and Astrophysics*, 11, 687
- Lattimer, J. M. 2011, *Ap&SS*, 336, 67
- Lattimer, J. M. & Prakash, M. 2001, *ApJ*, 550, 426
- 2007, *Phys. Rep.*, 442, 109
- 2010, *ArXiv e-prints*
- Lattimer, J. M., Prakash, M., Masak, D., & Yahil, A. 1990, *ApJ*, 355, 241
- Lattimer, J. M. & Swesty, D. 1991, *Nuclear Physics A*, 535, 331
- Law, D. R., Majewski, S. R., Skrutskie, M. F., Carpenter, J. M., & Ayub, H. F. 2003, *AJ*, 126, 1871
- MacEachern, S. N. & Berliner, L. M. 1994, *The American Statistician*, 48, 188
- Marconi, M., Caputo, F., Di Criscienzo, M., & Castellani, M. 2003, *ApJ*, 596, 299
- McClintock, J. E., Narayan, R., & Rybicki, G. B. 2004, *ApJ*, 615, 402
- McDonald, I., van Loon, J. T., Decin, L., Boyer, M. L., Dupree, A. K., Evans, A., Gehrz, R. D., & Woodward, C. E. 2009, *MNRAS*, 394, 831
- Méndez, M. & Belloni, T. 2007, *MNRAS*, 381, 790
- Miller, M. C., Lamb, F. K., & Psaltis, D. 1998, in *The Active X-ray Sky: Results from BeppoSAX and RXTE*, ed. L. Scarsi, H. Bradt, P. Giommi, & F. Fiore, 123–+
- Misner, C. W., Thorne, K. S., & Wheeler, J. A. 1973, *Gravitation*
- Müller, H. & Serot, B. D. 1996, *Nuclear Physics A*, 606, 508
- Müther, H., Prakash, M., & Ainsworth, T. L. 1987, *Physics Letters B*, 199, 469
- Nice, D. J., Splaver, E. M., & Stairs, I. H. 2004, in *IAU Symposium, Vol. 218, Young Neutron Stars and Their Environments*, ed. F. Camilo & B. M. Gaensler, 49
- Olofsson, J., Juhász, A., Henning, T., Mutschke, H., Tamanai, A., Moór, A., & Ábrahám, P. 2012, *A&A*, 542, A90
- Oppenheimer, J. R. & Volkoff, G. M. 1939, *Physical Review*, 55, 374
- Özel, F. 2006, *Nature*, 441, 1115
- Özel, F., Güver, T., & Psaltis, D. 2009, *ApJ*, 693, 1775
- Piotto, G. et al. 2002, *A&A*, 391, 945
- Pons, J. A., Walter, F. M., Lattimer, J. M., Prakash, M., Neuhäuser, R., & An, P. 2002, *ApJ*, 564, 981
- Prakash, M., Cooke, J. R., & Lattimer, J. M. 1995, *Phys. Rev. D*, 52, 661
- Prakash, M., Lattimer, J. M., & Ainsworth, T. L. 1988, *Physical Review Letters*, 61, 2518
- Predehl, P. & Schmitt, J. H. M. M. 1995, *A&A*, 293, 889
- Rajagopal, M. & Romani, R. W. 1996, *ApJ*, 461, 327
- Recio-Blanco, A. et al. 2005, *A&A*, 432, 851
- Rees, R. F. & Cudworth, K. M. 1991, *AJ*, 102, 152
- Rees, Jr., R. F. 1996, in *Astronomical Society of the Pacific Conference Series, Vol. 92, Formation of the Galactic Halo...Inside and Out*, ed. H. L. Morrison & A. Sarajedini, 289
- Romani, R. W. 1987, *ApJ*, 313, 718
- Rosenberg, A., Piotto, G., Saviane, I., & Aparicio, A. 2000, *A&AS*, 144, 5
- Rutledge, R. E., Bildsten, L., Brown, E. F., Pavlov, G. G., & Zavlin, V. E. 1999, *ApJ*, 514, 945
- 2001a, *ApJ*, 559, 1054
- 2001b, *ApJ*, 551, 921
- 2002, *ApJ*, 578, 405
- Sandquist, E. L., Gordon, M., Levine, D., & Bolte, M. 2010, *AJ*, 139, 2374
- Sato, K. 1979, *Progress of Theoretical Physics*, 62, 957
- Servillat, M., Heinke, C. O., Ho, W. C. G., Grindlay, J. E., Hong, J., van den Berg, M., & Bogdanov, S. 2012, *MNRAS*, 2965
- Servillat, M., Webb, N. A., & Barret, D. 2008, *A&A*, 480, 397
- Shen, G., Horowitz, C. J., & Teige, S. 2010a, *Phys. Rev. C*, 82, 015806
- 2010b, *Phys. Rev. C*, 82, 045802
- Steiner, A. W., Lattimer, J. M., & Brown, E. F. 2010, *ApJ*, 722, 33
- 2012, *ArXiv e-prints*
- Strickler, R. R., Cool, A. M., Anderson, J., Cohn, H. N., Lugger, P. M., & Serenelli, A. M. 2009, *ApJ*, 699, 40
- Suleimanov, V., Poutanen, J., Revnivtsev, M., & Werner, K. 2011a, *ApJ*, 742, 122
- Suleimanov, V., Poutanen, J., & Werner, K. 2011b, *A&A*, 527, A139
- Taylor, J. H. & Weisberg, J. M. 1989, *ApJ*, 345, 434
- Testa, V., Corsi, C. E., Andreuzzi, G., Iannicola, G., Marconi, G., Piersimoni, A. M., & Buonanno, R. 2001, *AJ*, 121, 916
- Valenti, E., Ferraro, F. R., & Origlia, L. 2007, *AJ*, 133, 1287
- van de Ven, G., van den Bosch, R. C. E., Verolme, E. K., & de Zeeuw, P. T. 2006, *A&A*, 445, 513
- van Paradijs, J., Verbunt, F., Shafer, R. A., & Arnaud, K. A. 1987, *A&A*, 182, 47
- Verbunt, F., Belloni, T., Johnston, H. M., van der Klis, M., & Lewin, W. H. G. 1994, *A&A*, 285, 903
- Walter, F. M., Eisenbeiß, T., Lattimer, J. M., Kim, B., Hambaryan, V., & Neuhäuser, R. 2010, *ApJ*, 724, 669
- Wang, Z., Breton, R. P., Heinke, C. O., Deloye, C. J., & Zhong, J. 2011, *ArXiv e-prints*
- Webb, N. A. & Barret, D. 2007, *ApJ*, 671, 727
- Weissenborn, S., Chatterjee, D., & Schaffner-Bielich, J. 2012, *Nuclear Physics A*, 881, 62
- Wiringa, R. B., Fiks, V., & Fabrocini, A. 1988, *Phys. Rev. C*, 38, 1010
- Woodley, K. A. et al. 2012, *AJ*, 143, 50
- Zamfir, M., Cumming, A., & Galloway, D. K. 2012, *ApJ*, 749, 69
- Zavlin, V. E., Pavlov, G. G., & Shibbanov, Y. A. 1996, *A&A*, 315, 141